Bioactive Materials 60 (2026) 456–471

Contents lists available at ScienceDirect

Bioactive Materials

journal homepage: www.keaipublishing.com/en/journals/bioactive-materials

Cord blood natural killer cell-derived extracellular vesicles inhibit Zika virus infectivity through ITGB2/perforin-mediated envelope disruption in vitro and in vivo

Chen Cheng [a,1], Ru Li [b,1], Tianwang Guan [a], Haowei Li [b], Luping Cheng [b], Min Zou [b,*], Shuwen Liu [b,c,**], Caiwen Ou [a,***]

[a] The Tenth Affiliated Hospital (Dongguan People's Hospital), Southern Medical University, Dongguan, 523059, China
[b] Guangdong Provincial Key Laboratory of New Drug Screening, School of Pharmaceutical Sciences, Southern Medical University, Guangzhou, 510515, China
[c] State Key Laboratory of Multi-organ Injury Prevention and Treatment, MOE Key Laboratory of Infectious Diseases Research in South China, Southern Medical University, Guangzhou, 510515, China

A B S T R A C T

Zika virus (ZIKV) can traverse the placental barrier, leading to fetal microcephaly and congenital zika syndrome (CZS). The viral E protein mediates host-cell interactions and infection. Here, we demonstrated that cord blood natural killer cell-derived extracellular vesicles (CBNK-EVs) potently inhibit ZIKV infection in vitro without compromising cellular viability. Mechanistically, CBNK-EVs engage ZIKV through ITGB2, a surface-enriched integrin that interacts with the viral E protein, facilitating nanoparticle-virion contact or membrane fusion. This interaction triggers antiviral activity via perforins within extracellular vesicles (EVs), resulting in diminished viral infectivity. Notably, CBNK-EVs not only effectively crossed the placental barrier to protect fetuses from ZIKV-induced pathologies, but also reduced the ZIKV burden in IFN-deficient murine models and decreased CZS incidence and mortality. Additionally, either blockade of ITGB2 with a monoclonal antibody or chelation of Ca^{2+} with EGTA impaired the anti-ZIKV activity of CBNK-EVs. Collectively, our findings identified CBNK-EVs as natural antiviral nanoparticles that play a pivotal role in curbing ZIKV infection and vertical transmission, offering a promising therapeutic strategy against congenital ZIKV-related complications.

1. Introduction

Zika virus (ZIKV) is a positive-sense RNA arbovirus belonging to the Flaviviridae family, with reported local transmission in over 80 countries worldwide [1]. Mosquito-borne, mother-to-child, and blood-borne transmission are the principal routes of ZIKV dissemination. Vertical transmission significantly increases the risk of congenital Zika syndrome (CZS) in the fetus, which manifests as microcephaly (reduced cranial size), ventriculomegaly (enlarged cerebral ventricles), calcification in subcortical regions, and neurological dysfunction [2]. In 2016, the WHO declared the ZIKV outbreak a public health emergency of international concern. ZIKV infection in pregnant women can lead to congenital anomalies and fetal death [3]. Mechanistically, ZIKV infects placental cells by degrading tight junction proteins or traversing the placental barrier via immune-evading tunneling nanotubes [4]. ZIKV spreads to the brain, efficiently infecting and causing CZS in fetuses [5]. In addition, ZIKV infection in adults has been linked to Guillain–Barré syndrome [6]. Over the past decade, the scientific community has made progress in developing vaccines and small-molecule therapeutics against ZIKV infection [7]. However, as a critical infectious disease, ZIKV outbreaks continue to occur frequently in tropical and subtropical regions, and available treatments for ZIKV infection remain limited.

Extracellular vesicles (EVs) are nanoscale vesicles secreted by cells that carry functional components, such as bioactive proteins and small RNAs, which are characteristic of their parent cells [8]. Stem cell-derived EVs have entered clinical trials for their anti-inflammatory and tissue-repair properties [9,10]. Natural killer (NK) cell-derived EVs (NK-EVs) exhibit high biocompatibility, low immunogenicity, and inherent homing capabilities [11]. NK-EVs contain unique cargo proteins that are characteristic of NK cells, including perforins, granzymes,

Peer review under the responsibility of editorial board of Bioactive Materials.
* Corresponding author.
** Corresponding author. Guangdong Provincial Key Laboratory of New Drug Screening, School of Pharmaceutical Sciences, Southern Medical University, Guangzhou, 510515, China.
*** Corresponding author.
E-mail addresses: zoum2000@smu.edu.cn (M. Zou), liusw@smu.edu.cn (S. Liu), oucaiwen@smu.edu.cn (C. Ou).
[1] C.C. and R.L. contributed equally to this study.

https://doi.org/10.1016/j.bioactmat.2026.01.030
Received 18 November 2025; Received in revised form 14 January 2026; Accepted 19 January 2026
Available online 31 January 2026

and membrane markers, which have been extensively studied for anti-tumor applications [12]. Additionally, NK-EVs may possess immunomodulatory and anti-SARS-CoV-2 functions, although their underlying mechanisms remain unclear [13]. Compared with adult peripheral NK cells, human umbilical cord blood-derived NK cells (CBNKs) provide ethical advantages and lower heterogeneity for clinical procurement. The high proportion and proliferative potential of CBNKs make them ideal donor cells for CAR-NK therapy [14], which is advantageous for obtaining many CBNK-EVs. The roles and mechanisms of CBNK-EVs in ZIKV infection were investigated in this study.

In this study, we found that CBNK-EVs exhibit potential anti-ZIKV activity in both Vero-E6 and BHK-21 cells. Further analysis revealed

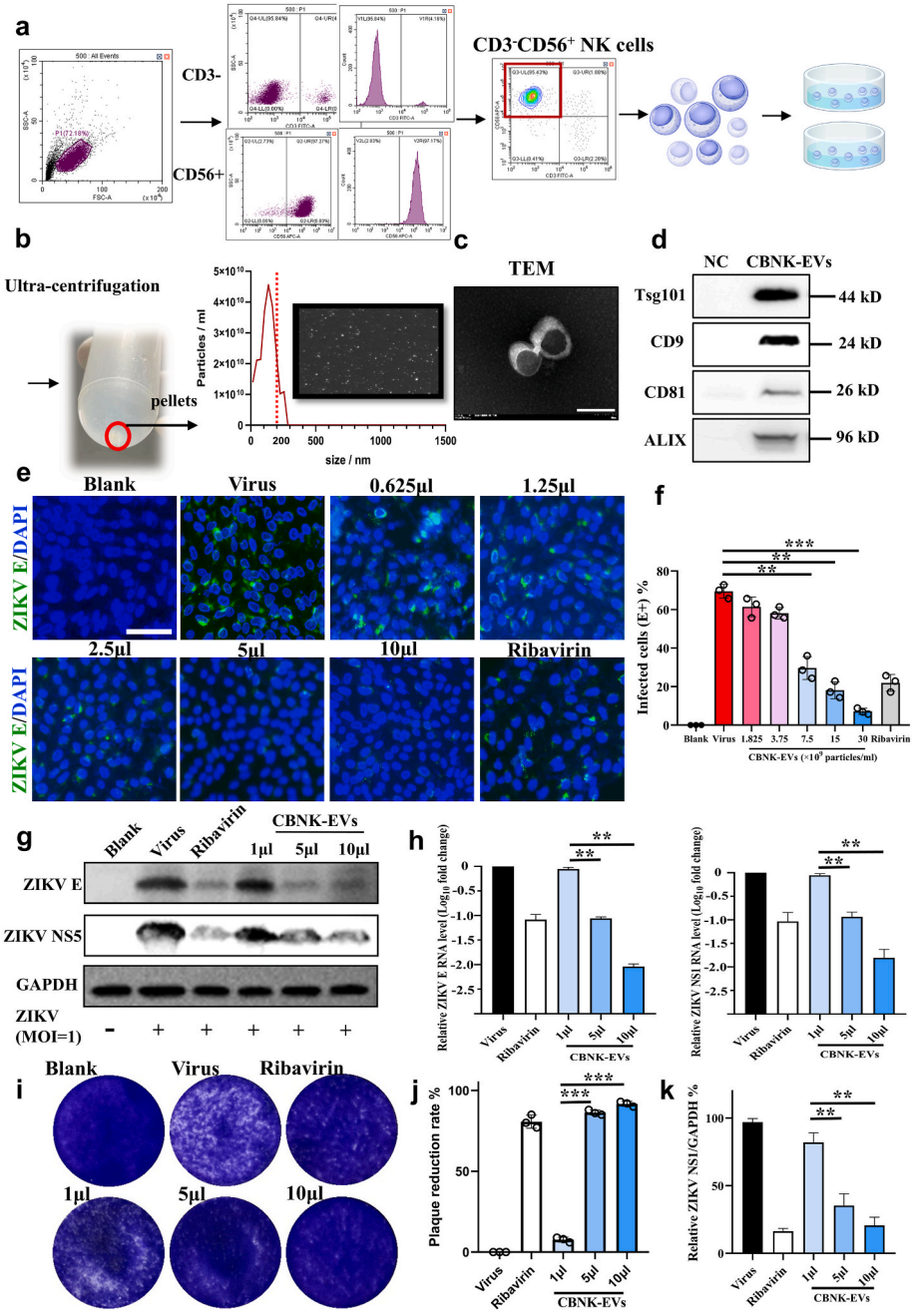

Fig. 1. Characterization and anti-ZIKV activity of CBNK-EVs. (a) Isolation of CBNK cells by fluorescence-activated cell sorting. **(b)** Collection of CBNK-EVs and NTA for size distribution and concentration. **(c)** Morphological observation of CBNK-EVs by transmission electron microscopy, scale bar:100 nm. **(d)** WB analysis of specific markers for CBNK-EVs. **(e)** Anti-ZIKV activity of CBNK-EVs assessed by immunofluorescence. Vero-E6 cells were seeded in 12-well plates at 1×10^5 cells per well one day prior to experiments. Cells were pretreated with varying volumes of CBNK-EVs (stock concentration: 3×10^{11} particles/mL) for 1 h to achieve the indicated final particle counts, followed by infection with ZIKV (MOI = 1) for 24 h in the presence of fresh medium containing the same EVs. ZIKV-infected cells were quantified by counting E protein-positive cells in three random fields by two independent investigators. Scale bar, 40 μm. **(f)** Statistical analysis of the data presented in (e) panel. **(g)** Vero-E6 cells were treated as in (e) and infected with ZIKV (MOI = 1) for 24 h. **(h)** ZIKV E and NS1 RNA levels were detected by quantitative RT-PCR. Data were normalized to GAPDH, log10-transformed, and presented as fold change compared to the virus control group (set to 1). Negative values indicate inhibition of viral replication. **(i)** Plaque reduction assay assessing the antiviral activity of CBNK-EVs against ZIKV. **(j)** Statistical analysis of the percentage of plaque reduction. **(k)** ZIKV NS5 protein levels in (g) were analyzed by Western blot. Data in panels (f, h, j and k) are presented as mean ± SD (n = 3). *P < 0.05, **P < 0.01, ***P < 0.001.

that CBNK-EVs destabilized ZIKV membranes through direct interactions with viral particles, thereby inhibiting ZIKV adsorption and cellular entry. In vivo studies have suggested that CBNK-EVs prophylactically mitigate ZIKV infection and vertical transmission, and reduce microcephaly and neurological infections in murine pups. Mechanistically, this antiviral activity was linked to ITGB2 on CBNK-EVs, which mediates EV-ZIKV interactions by binding to the viral envelope (E) protein. The abundance of perforins and granzymes within CBNK-EVs contributes to decreased viral activity, suggesting that these proteins are putative active mediators of ZIKV neutralization. We demonstrate that CBNK-EVs serve as safe and effective nanoparticles for combating ZIKV infection and CZS damage.

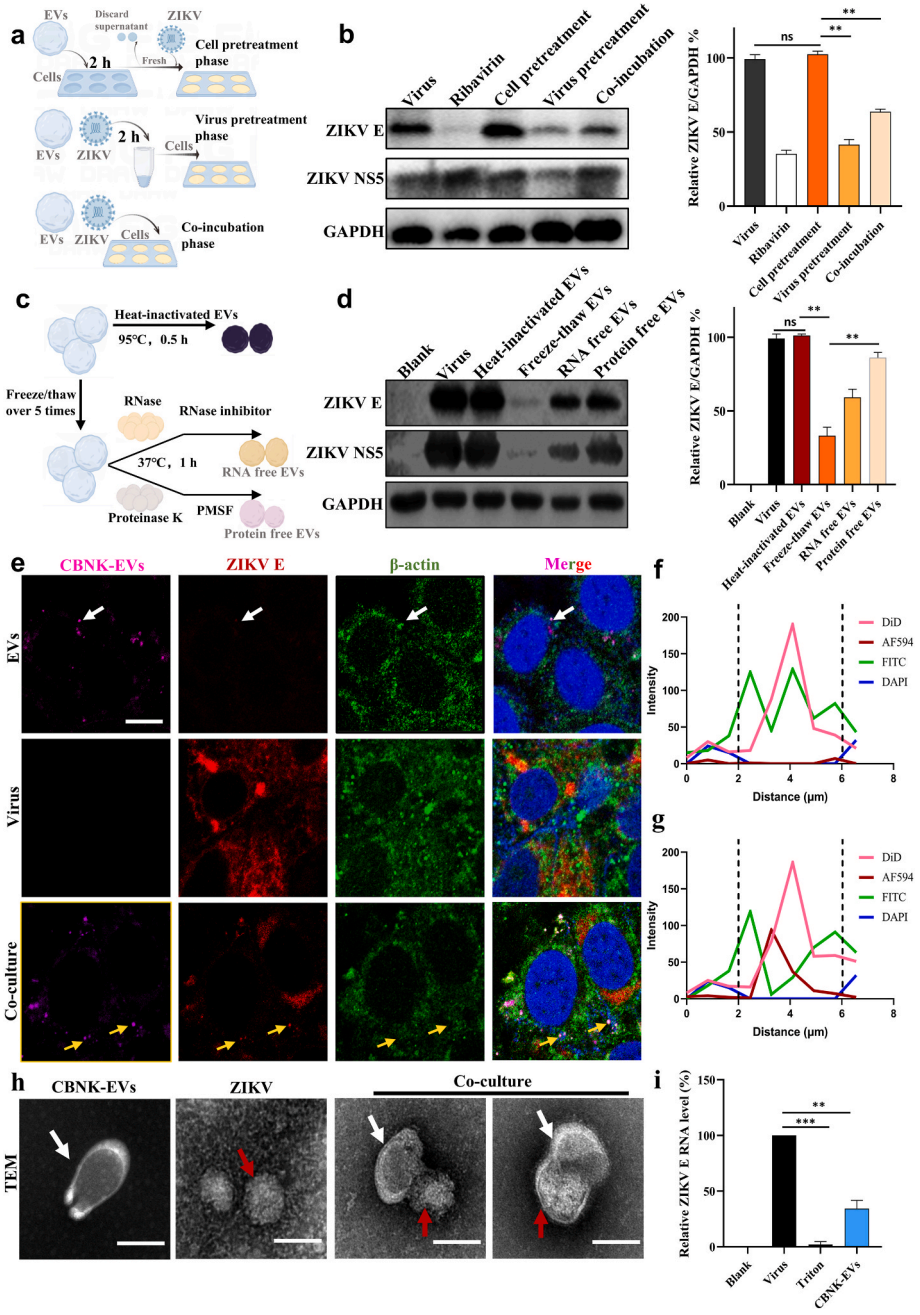

Fig. 2. Functional components and mechanisms of CBNK-EVs in combating ZIKV infection. (a) Schematic of three treatment modalities: **1)** pre-treatment of cells with CBNK-EVs, **2)** pre-treatment of virus with CBNK-EVs, and **3)** co-incubation of CBNK-EVs with ZIKV. **(b)** Vero-E6 cells were seeded at 1×10^5 cells per well in 12-well plates and subjected to the treatments outlined in (a), followed by infection with ZIKV (MOI = 1) for 1 h. After 48 h, ZIKV E and ZIKV NS5 protein levels were analyzed by Western blot (left). Densitometric analysis of the protein bands is shown (right, n = 3). **(c)** Schematic workflow for functional component inactivation in CBNK-EVs (e.g., by heat, protease, or nuclease treatment). **(d)** Vero-E6 cells were treated with inactivated CBNK-EVs as per the scheme in (c), followed by infection with ZIKV (MOI = 1) for 1 h. ZIKV E and ZIKV NS5 protein levels were analyzed by Western blot after 24 h. Densitometric analysis of the protein bands is shown (right, n = 3). **(e)** Represent images of the co-localization of CBNK-EVs, ZIKV E and host cells by confocal microscope, scale bar: 5 μm. **(f)** Fluorescence intensity of CBNK-EV and β-actin co-localization signals (white arrows) in the EVs group. **(g)** Fluorescence co-localization signals (yellow arrows) of CBNK-EVs and ZIKV in the co-culture group. **(h)** TEM images of CBNK-EVs, ZIKV particles, and their interactions. Scale bar: 100 nm. **(i)** Membrane disruption assay. ZIKV particles were co-incubated with CBNK-EVs, followed by treatment with micrococcal nuclease to digest unprotected RNA. Intact viral RNA, indicative of membrane integrity, was then measured by RT-qPCR targeting the ZIKV E. Mean ± SD (n = 3). $^{**}P < 0.01$, $^{***}P < 0.001$ (one-way ANOVA).

2. Results

2.1. Characterization of CBNK-EVs

We initially isolated mononuclear cells from umbilical cord blood and then purified $CD3^{-}CD56^{+}$ CBNK cells via fluorescence-activated cell sorting (FACS, Fig. 1a). Conditioned media from cultured CBNK cells were collected and CBNK-EVs were isolated using differential ultracentrifugation. Nanoparticle tracking analysis (NTA) revealed that CBNK-EVs exhibited a predominant size distribution below 200 nm, with the highest particle count observed at approximately 100 nm (Fig. 1b). Transmission electron microscopy (TEM) confirmed the characteristic cup-shaped morphology of the vesicles (Fig. 1c). Western blot (WB) demonstrated significant enrichment of exosomal markers, including CD9, CD81, TSG101, and ALIX in CBNK-EVs, validating their identity (Fig. 1d). Calnexin was not detected in CBNK-EVs, further confirming the good purity of the isolated extracellular vesicles [15] (Fig. S1a). CBNK-EVs were diluted with EVs-free PBS to the desired concentration and stored at −80 °C for subsequently experiments.

2.2. Anti-ZIKV activity of CBNK-EVs

To evaluate the antiviral potential of CBNK-EVs, we assessed their cytotoxicity in epithelial cells. Purified CBNK-EVs (the maximum yield of EVs routinely achieved in our laboratory is 10^{12} particles/mL) showed no adverse effects on the viability of Vero E6 or BHK-21 cells (Fig. S1b and S1c). To establish an effective dosing regimen, we targeted an initial EV-to-cell ratio of 1000:1 (10^{8}-10^{9} particles/mL). Given the robust antiviral activity observed in Vero E6 and BHK-21 cells at 3×10^{9} particles/well (Fig. S1d), a working concentration of 3×10^{11} particles/mL was ultimately selected for all subsequent assays. Furthermore, the anti-ZIKV effect was found to be dose-dependent, with significant inhibition becoming evident at concentrations around 10^{9} particles/mL (Fig. 1e and f). This was evidenced by decreased expression of ZIKV E protein and nonstructural 5 (NS) proteins (Fig. 1g and k), and suppressed ZIKV E and NS1 RNA replication (Fig. 1h). NS proteins play an important role in neuropathogenesis induced by ZIKV [16]. The plaque reduction assay visually demonstrates that CBNK-EVs effectively reduce ZIKV infectivity in a dose-dependent manner (Fig. 1i and j). Notably, CBNK-EVs exhibited less inhibitory activity against another type of flavivirus dengue virus (DENV) even at 10^{10} particles/mL (Fig. S1e and S1f), suggesting a preferential mechanism targeting ZIKV.

2.3. CBNK-EVs mediate ZIKV membrane instability

To elucidate the antiviral mode of action, we designed three distinct treatment protocols (Fig. 2a): (1) Cell pretreatment phase, where cells were pre-exposed to EVs and washed prior to infection; (2) Virus pretreatment phase, where EVs were pre-incubated with ZIKV particles before infection; and (3) Co-incubation phase, where EVs and ZIKV were added simultaneously. Western blot analysis revealed that the virus pretreatment group exhibited the most significant reduction in ZIKV E protein levels, indicating impaired viral infectivity. In contrast, cell pretreatment provided no protection, suggesting that CBNK-EVs do not primarily function by modulating host cell resistance but rather through direct virucidal activity (Fig. 2b). Consistent with this, plaque assays confirmed that pre-incubating ZIKV with CBNK-EVs significantly reduced viral titers (Fig. S1g and S1h). Inactivating EV components via heat or specific enzymes allows for the functional dissection of their antiviral cargo [17], as illustrated in Fig. 2c. The antiviral potency of these modified EVs was then evaluated using the virus pretreatment protocol. Results revealed that protein-containing, RNA-free CBNK-EVs showed anti-viral activity, whereas EVs with inactivated proteins exhibited weaker antiviral capabilities, implicating EV-associated proteins as key mediators of anti-ZIKV activity (Fig. 2d). Markedly, the antiviral potency of CBNK-EVs remained unaltered even after multiple freeze-thaw cycles, underscoring their structural and functional robustness. EVs were taken up by host cells (Fig. 2e and f), and CBNK-EVs co-localized with ZIKV and reduced E protein positive area (Fig. 2e and g). The observed co-localization of punctate fluorescence showed that the two entities may interact during the brief pre-incubation period. TEM imaging provided a more intuitive view of the interactions between CBNK-EVs and ZIKV particles. Two modes were observed, direct binding and membrane fusion (Fig. 2h). Internalized CBNKEV-ZIKV complexes co-localized within cells, but failed to establish a productive infection (Fig. 2e and g). Given that we previously discovered that CBNK-EVs exhibit good antiviral activity only when they interact with viral particles (Fig. 2b), we hypothesized that this interaction directly damages the virus structure. The integrity of the ZIKV envelope, a single-stranded positive-sense RNA virus, is critical for protecting its genomic RNA. Micrococcal nuclease degrades the viral RNA following envelope damage, whereas RNA within intact virions remains protected and quantifiable by real-time fluorescence quantitative PCR (RT-qPCR) [18]. The result showed that viral RNA replication level was significantly reduced upon CBNK-EV treatment, and confirmed that CBNK-EVs led to the destruction of the ZIKV envelope and exposure of the viral RNA (Fig. 2i).

2.4. CBNK-EVs could cross the placental barrier and reduce ZIKV vertical transmission

Notably, ZIKV can cross the placental barrier and infect the fetus, causing abnormalities in the brain and head. Therefore, the ability to cross the placental barrier is important for the anti-ZIKV activity. The process of EVs crossing biological barriers and accumulating in protected organs like the brain typically takes several hours following intravenous injection [19]. In this study, EV signals were detectable in the lower abdomen 4 h post-injection (Fig. 3a and b). The EV signal in the lower abdomen gradually faded over time and had largely diminished to background levels by the 24-h time point (Fig. S2a and S2b). Ex vivo signal detection revealed that CBNK-EVs were significantly enriched in the uterus and fetus after intravenous injection, as confirmed by fluorescence imaging of DID-labeled EVs in the uterine and fetal tissues (Fig. 3c, d and 3e). Ex vivo imaging also confirmed the retention of CBNK-EVs in the uterus (Fig. S2c) and fetuses (Fig. S2d) for several hours, prior to a marked decline in signal intensity by the 24-h time point (Fig. S2e). Simultaneously, CBNK-EVs demonstrated a favorable safety profile in both the mothers and the fetuses (Fig. S3a and S3b). Continuous injection of high concentrations of CBNK for 2 weeks did not cause abnormal liver and kidney function in pregnant mice (Fig. S3c and S3d) or tissue pathology (Fig. S3e). Therefore, it is crucial to determine whether CBNK-EVs exhibit antiviral activity in vivo. IFNAR mAb (10 mg/kg) was used to block the innate immune response and facilitate the establishment of a ZIKV infection model in BALB/c mice. CBNK-EVs significantly protected against ZIKV-induced fetal damage, as evidenced by a reduction in ZIKV RNA replication in the placenta (Fig. 3f)., as well as decreased copies of ZIKV E RNA in fetal head tissues (Fig. 3g). Compared to the heat-inactivated CBNK-EVs (CBNK-HI-EVs) group, CBNK-EVs markedly ameliorated the reduction in fetal head circumference (Fig. 3h) or microcephaly (Fig. S3f and S3g), which was associated with suppressed ZIKV infection in the fetuses. Histopathological analysis revealed preserved cytoarchitecture in the hippocampal and cortical regions, with minimal ZIKV infection observed in the neural cells (quantified by counting ZIKV E-positive cells, Fig. 3i-k). Multiplex immunofluorescence staining for Nestin (neural progenitor cells) and ZIKV E protein (infected cells) demonstrated that CBNK-EVs also significantly reduced ZIKV infection of neural progenitor cells (Fig. 4a). Our experiments confirmed that CBNK-EVs, as safe and specific ZIKV-inactivating nanoparticles, could effectively reduce the ZIKV load in fetal mice and decrease CZS occurrence.

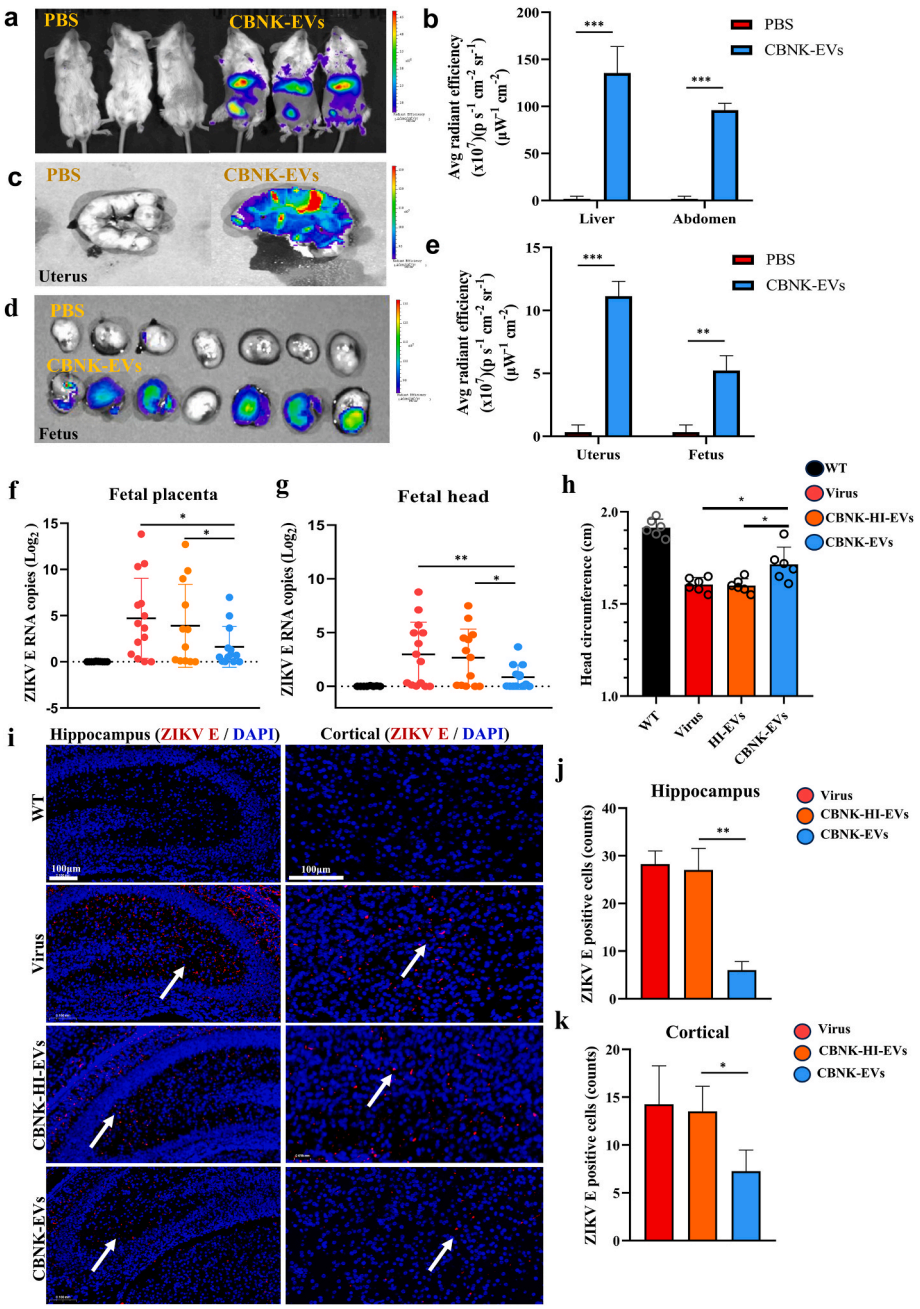

Fig. 3. Protective effects of CBNK-EVs against ZIKV infection in fetal mice. (a) In vivo imaging of pregnant mice at 4 h post-intravenous injection of DiD-labeled CBNK-EVs (6×10^{12} particles/mL, 200 μl per mouse). **(b)** Relative quantitative analysis of fluorescence intensity in the liver and lower abdomen from (a). **(c)** Representative image of CBNK-EV signals enriched in uterine tissues at 4 h time point. **(d)** Representative image showing transplacental migration and distribution of CBNK-EVs in fetus at 4 h time point. **(e)** Quantitative analysis of CBNK-EV fluorescence intensity in embryonic tissues from (d). **(f)** CBNK-EVs reduced ZIKV E RNA copies in placental tissues as measured by RT-qPCR. **(g)** CBNK-EVs significantly suppressed ZIKV E RNA levels in fetal heads. **(h)** CBNK-EVs ameliorated ZIKV-induced microcephaly, assessed by measuring the maximum head circumference. **(i)** Immunofluorescence staining of ZIKV E protein (red) in fetal hippocampal and cortical brain regions. Cell nuclei were stained with DAPI (blue). Scale bar: 100 μm. **(j)** Quantification of ZIKV E-positive cells in the hippocampus and **(k)** cortex from at least three random fields per sample. Data are presented as mean ± SD; n = 3 for (b, e, j, k), n = 14 for (f, g). *P < 0.05, **P < 0.01, ***P < 0.001 (one-way ANOVA).

2.5. *CBNK-EVs confer host-cell protection against ZIKV infection*

Neural progenitor cells are widely recognized as the preferred target for ZIKV infection within the nervous system [20]. We found that CBNK-EVs reduced viral invasion into fetal neural progenitor cells (Fig. 4a). This protective effect was associated with the ability of CBNK-EVs to directly attenuate viral infectivity, as reflected by decreased ZIKV RNA copies in placental tissues (Fig. 3f).

In a well-defined in vitro infection model, human placental trophoblasts cell line HTR-8/Svneo was challenged with ZIKV and simultaneously treated with either heat-inactivated EVs (CBNK-HI-EVs, negative control) or active CBNK-EVs. Following a 1-h incubation, both viral particles and EVs were removed, and the cells were maintained in 2 % FBS medium for 24 h before RNA extraction and sequencing. Principal component analysis showed clear separation among the three groups (Fig. S4a), and CBNK-EVs substantially rescued the ZIKV-induced disruption of the transcriptional landscape (Fig. S4b–S4e). To identify the molecular mechanisms underlying this protection, we performed

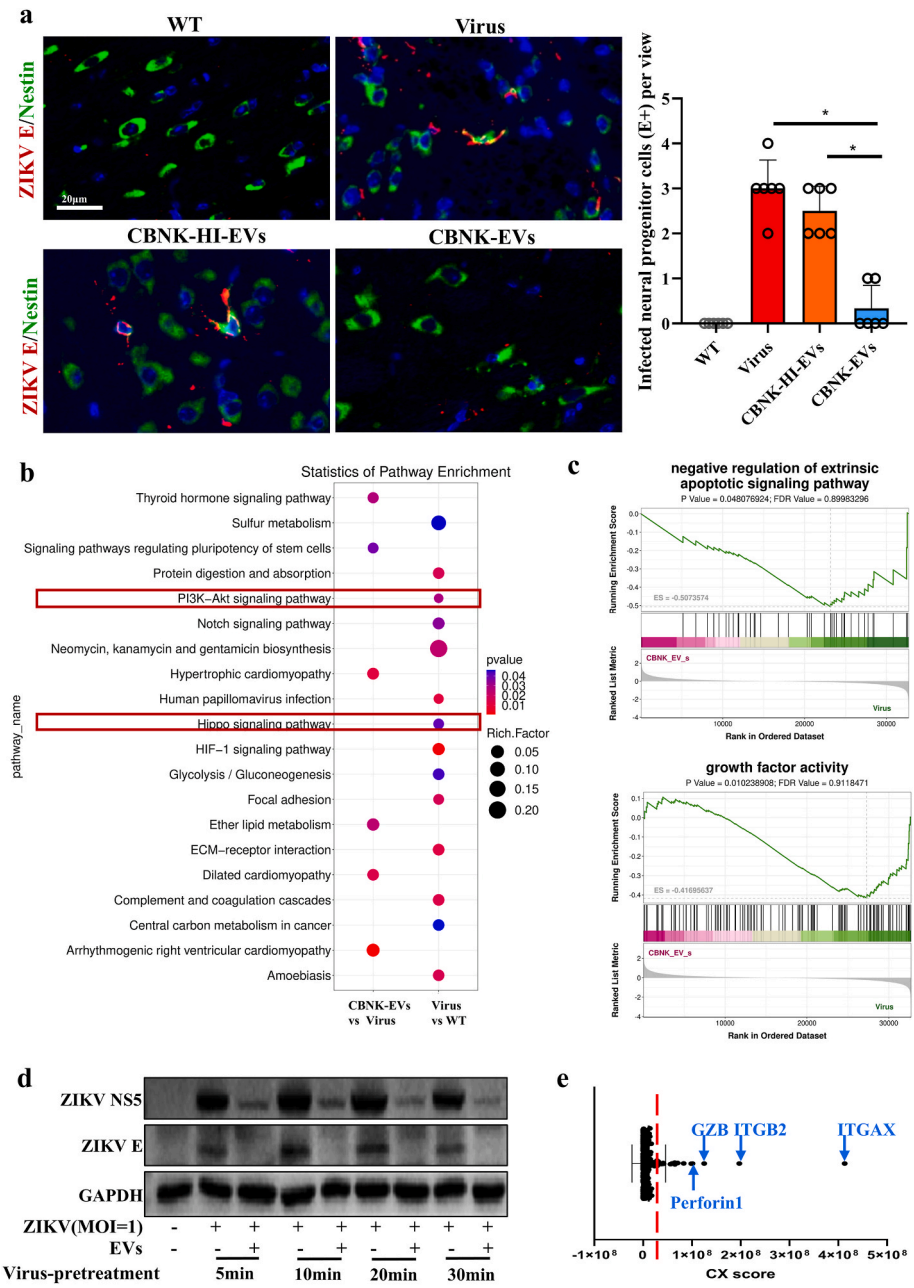

Fig. 4. CBNK-EVs rapidly impair ZIKV infectivity and protect host cells. (a) Multiplex immunohistochemical analysis of ZIKV infection in neural progenitor cells. Co-staining for Nestin (neural progenitor cells, green) and ZIKV E protein (red) was performed, and double-positive cells were quantified across six random fields, mean ± SD, *P < 0.05. Scale bar, 20 μm. **(b)** KEGG pathway enrichment bubble plot from RNA-seq of HTR-8/Svneo cells treated with CBNK-EVs (3×10^{11} particles/mL, 10 μl) and ZIKV (MOI = 1) for 1 h. **(c)** GSEA analysis of transcriptomic data from HTR-8/Svneo cells. **(d)** Western blot analysis of ZIKV E and ZIKV NS5 protein levels after co-incubation of ZIKV particles with CBNK-EVs for the indicated time periods (0–30 min) prior to infection. **(e)** The abundance of NK cell-associated proteins in CBNK-EVs. *P < 0.05 (one-way ANOVA).

RNA sequencing on HTR-8/Svneo cells from three groups: WT (uninfected), Virus, and ZIKV-infected treated with CBNK-EVs. We focused on signaling pathways that were significantly altered by ZIKV infection (Virus vs. WT) and subsequently rescued by CBNK-EVs treatment (CBNK-EVs vs. Virus). KEGG pathway analysis further revealed that CBNK-EVs significantly restored the dysregulation of both Hippo and PI3K-Akt signaling pathways (Fig. 4b). Notably, the ZIKV-elicited reduction in infected cell death previously reported by Li et al. was recapitulated in our study [21], plausibly attributable to the ZIKV-mediated upregulation of anti-apoptotic genes (Fig. 4c). Collectively, these data demonstrate the rapid antiviral action of CBNK-EVs. To further delineate the kinetics of this effect, we performed a time-resolved pre-incubation assay and found that a mere 5-min exposure of ZIKV particles to CBNK-EVs was sufficient to compromise viral infectivity, leading to a pronounced reduction in ZIKV NS5 and ZIKV E protein level (Fig. 4d). This prompt virucidal effect prompted us to investigate the underlying mechanism. Given our prior evidence suggesting proteins as the primary active components of CBNK-EVs (Fig. 2c and d), proteomic profiling of CBNK-EVs was used and several highly abundant NK-related proteins were identified (Fig. 4e and Supplementary Table 2).

2.6. Components and mechanism of CBNK-EVs against ZIKV infection

Notably, integrins were abundant in the CBNK-EVs, with ITGAX and ITGB2 being particularly enriched (Fig. 4e and S4f). In addition, granzymes and perforins were highly expressed (Fig. 5a) and both showed anti-ZIKV activity in vitro (Fig. 5b). To determine whether perforins within CBNK-EVs mediate viral disruption in micrococcal nuclease digestion assay, we chelated Ca^{2+} with EGTA to prevent perforin activation [22] (the calcium ion concentration in DMEM is approximately 1.8 mM generally). Under these conditions, the ability of CBNK-EVs to disrupt the integrity of ZIKV virion was markedly attenuated (Fig. 5c). Among perforin targeting siRNAs transfected into CBNK cells, siRNA3 demonstrated the most efficient knockdown (Fig. 5d and e) and exhibited dose-dependent efficacy (Fig. S4g), and was therefore selected

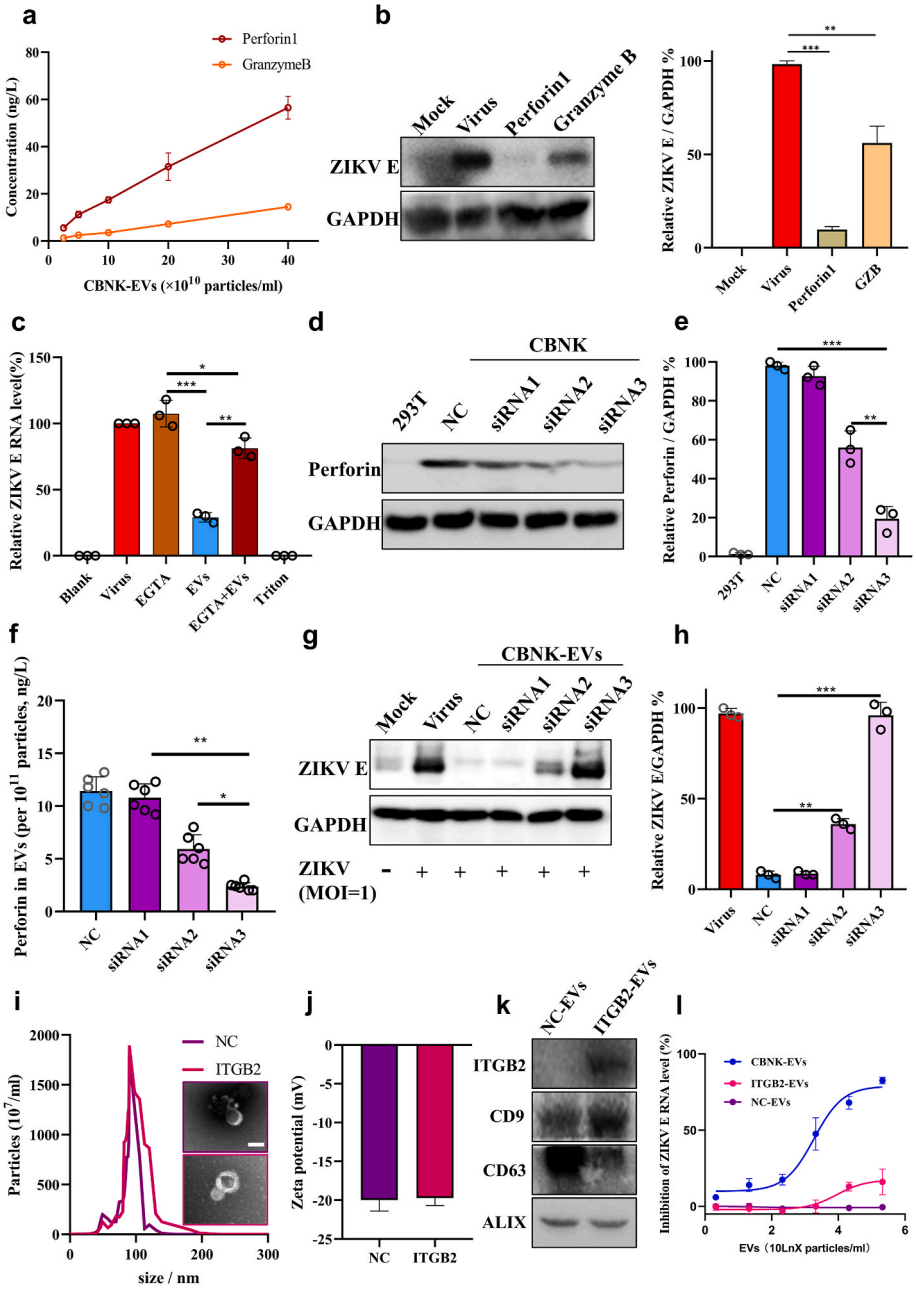

Fig. 5. Perforin mediates the direct virion-disrupting activity of CBNK-EVs. (a) Quantification of perforin and granzyme B in CBNK-EVs by ELISA. **(b)** Vero-E6 cells were infected with ZIKV (MOI = 1) after pre-incubation of viral particles with 40 ng/L of recombinant perforin or granzyme B for 2 h. ZIKV E protein levels were assessed by Western blot after 24 h, densitometric analysis of the protein bands is shown (right, n = 3). **(c)** CBNK-EVs were pre-incubated with ZIKV in the presence or absence of 10 mM EGTA, followed by micrococcal nuclease digestion. Protected ZIKV E RNA was quantified by RT-qPCR to assess virion integrity. **(d)** Western blot analysis of perforin expression in CBNK cells after transfection with the indicated siRNAs. **(e)** Quantification of perforin levels from (d). **(f)** Perforin levels in CBNK-EVs collected from control or perforin-knockdown cells, measured by ELISA and normalized to particle count (per 10^{11} particles, n = 6). **(g)** Vero-E6 cells were infected with ZIKV (MOI = 1) that had been pre-incubated with control or perforin-knockdown CBNK-EVs. ZIKV E protein levels were evaluated by Western blot. **(h)** Analysis of ZIKV E protein levels from (g). **(i)** Characterization of ITGB2-EVs and control EVs from 293T cells by NTA and TEM. Scale bar, 100 nm. **(j)** Zeta potential measurements of ITGB2-EVs and control EVs. **(k)** Western blot analysis of EV markers and ITGB2 expression in ITGB2-EVs and control EVs. **(l)** Antiviral activity of CBNK-EVs and ITGB2-EVs evaluated by cell-based ZIKV E protein ELISA. Data are presented as mean ± SD (n = 3). *P < 0.05, **P < 0.01, *P < 0.001 (one-way ANOVA).

for subsequent functional assays. The culture medium was replaced 8 h post-transfection, and EVs were harvested from the supernatants at another 48 h for subsequent functional assays. Results showed that CBNK-EVs derived from siRNA3-transfected cells contained lower perforin (Fig. 5f) and exhibited markedly diminished antiviral capacity upon co-incubation with ZIKV, as assessed by ZIKV E protein expression levels (Fig. 5g and h). Collectively, these data indicate that perforin is the principal pore-forming effector responsible for the rapid antiviral activity of CBNK-EVs. Integrins, such as ITGB4, could be important for ZIKV adsorption and entry [23]. We next overexpressed ITGAX or ITGB2 in 293T cells, which are normally refractory to ZIKV infection [24]. Notably, ITGB2 overexpression, but not ITGAX, was correlated with increased ZIKV RNA levels (Fig. S4h). This prompted us to ask whether ITGB2 on CBNK-EVs influences their antiviral activity. We therefore isolated EVs from 293T cells stably overexpressing ITGB2 (ITGB2-EVs, Fig. 5i-k) and evaluated their antiviral potency. However, ITGB2-EVs did not exhibit significant direct antiviral activity as CBNK-EVs (Fig. 5l), consistent with their lack of virucidal cargo such as perforin-1 and granzymes. And the marginal antiviral effects of ITGBW-EVs at high concentrations presumably is likely attributable to the competitive inhibition of cellular attachment sites [25].

Moreover, we observed that ITGB2 transfection enhanced the susceptibility of 293T cells to ZIKV (Fig. 6a). ITGB2-positive cells were more susceptible to infection and promoted viral dissemination between

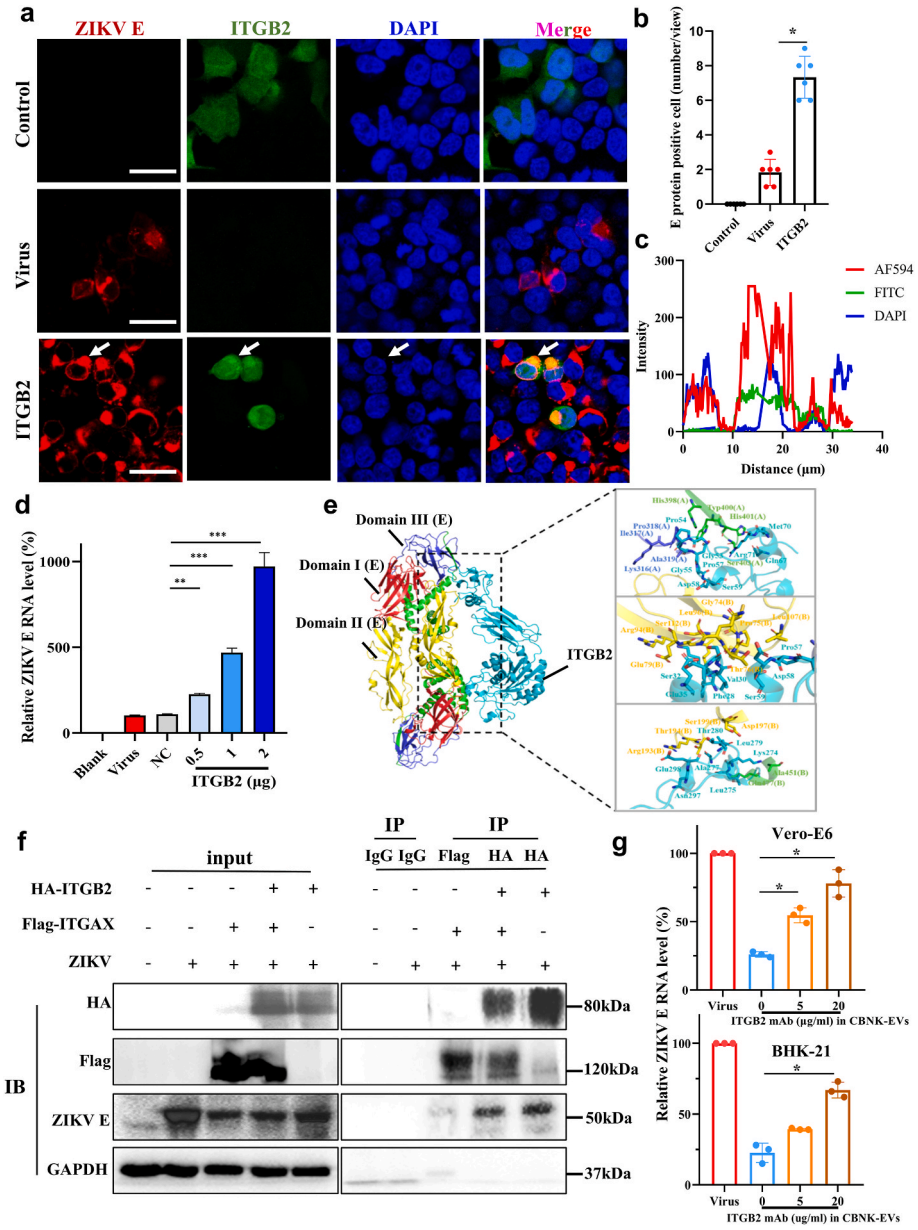

Fig. 6. ITGB2 facilitates CBNK-EVs binding to Zika virions and enhances cellular susceptibility to ZIKV. (a) Multicolor immunofluorescence staining of 293T cells transfected with ITGB2, showing co-localization (yellow) between ITGB2 (green) and ZIKV E protein (red). Scale bar: 20 μm. **(b)** Quantitative analysis of ZIKV E-positive 293T cells from (a). **(c)** Fluorescence intensity profile along white arrows in (a), indicating sites of ITGB2 and ZIKV E co-localization. **(d)** 293T cells were transfected with increasing amounts (0.5, 1, 2 μg) of ITGB2 plasmid and infected with ZIKV (MOI = 1) for 1 h. ZIKV RNA levels were measured by qPCR to assess infection susceptibility (mean ± SD, n = 3). **(e)** Molecular docking model predicting the interaction interface between ITGB2 and ZIKV E protein. **(f)** Co-IP assay in 293T cells, followed by immunoblotting with anti-ZIKV E protein antibody. **(g)** CBNK-EVs were pre-incubated with ITGB2 mAb (0, 5, 20 μg/mL) before being applied to Vero-E6 or BHK-21 cells. Cells were then infected with ZIKV (MOI = 1) for 1 h, and antiviral activity was assessed by measuring ZIKV RNA levels at 24 h post-infection. Data are presented as mean ± SD (n = 3 for d and g; n = 6 for b). *P < 0.05, **P < 0.01, ***P < 0.001 (one-way ANOVA).

cells (Fig. 6b). ITGB2-E protein co-localization was detected by confocal microscopy (Fig. 6c). ITGB2 significantly increased ZIKV RNA replication in a dose-dependent expression level of ITGB2 (Fig. 6d). Molecular docking simulations predicted a high-affinity interaction between ITGB2 and the ZIKV envelope (E) dimer. The E protein dimer adopts an anti-parallel conformation, with ITGB2 primarily interacting with domains II (yellow) and III (blue) of the E protein (Fig. 6e). A detailed analysis showed that ITGB2 residues 53–71 engage the DIII region (ZIKV E-A chain), and a composite pocket formed by Ala277-Glu298 of ITGB2 anchors the DII/DIII hinge of the E-B chain via hydrogen bonds (Lys29-Glu79 and Asn297-Ser199) and a salt bridge (Glu298-Arg193). Co-IP experiments further confirmed the interaction between ITGB2 and ZIKV E proteins (Fig. 6f). To investigate whether ITGB2 was the key protein responsible for the anti-ZIKV activity of CBNK-EVs, a monoclonal antibody against ITGB2 was used to block the EVs. The anti-ITGB2 antibody weakened the ability of CBNK-EV to reduce the

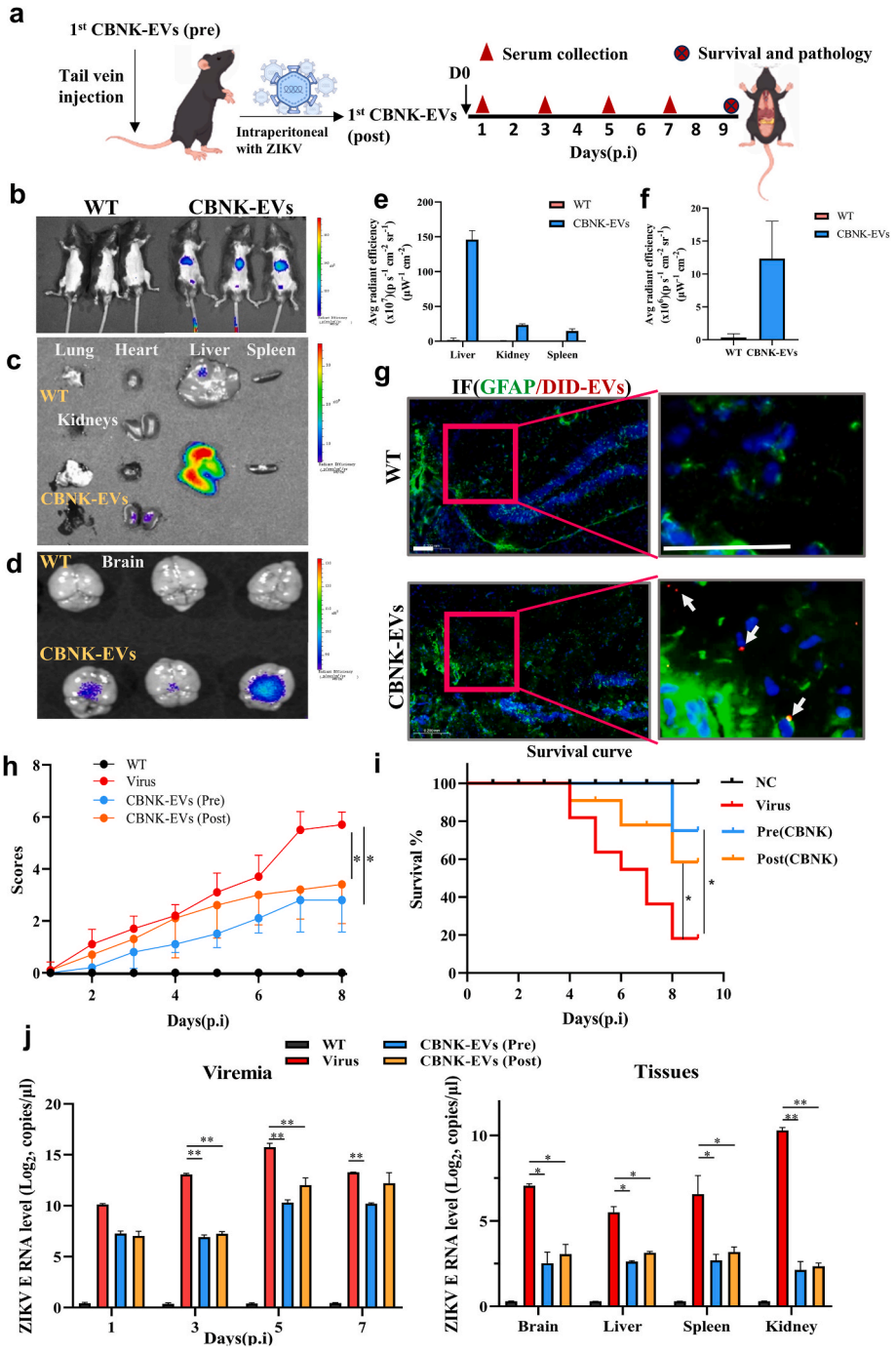

Fig. 7. CBNK-EVs cross the blood–brain barrier and attenuate ZIKV infection in AG6 mice. (a) Schematic timeline of the AG6 mouse experiment. Mice were intravenously administered CBNK-EVs (6×10^{12} particles in 200 μL PBS) via the tail vein, and viremia was monitored at indicated time points (n = 10). **(b)** In vivo imaging to monitor the biodistribution of CBNK-EVs in AG6 mice. **(c)** CBNK-EVs exhibited differential accumulation in the liver, kidneys, spleen and **(d)** brain. **(e)** Relative quantitative analysis of fluorescence intensity for EVs distribution in liver, kidneys, spleen and **(f)** brain (mean ± SD, n = 3). **(g)** Multicolor immunofluorescence staining showed the distribution of CBNK-EVs within the hippocampus. Scale bar: 100 μm. **(h)** Behavioral scoring analysis of AG6 mice post-ZIKV challenge (mean ± SD, n = 10). **(i)** Survival analysis of AG6 mice post-ZIKV challenge (n = 10). **(j)** Viremia at various time points and viral loads in different tissues were quantified by qPCR (mean ± SD, n = 10). *P < 0.05, **P < 0.01, log-rank test for (i) and one-way ANOVA for other panels.

replication of ZIKV RNA, as observed in various epithelial cells (Fig. 6g). Collectively, our results indicated that ITGB2 mediates initial docking between CBNK-EVs and ZIKV, positioning the encapsulated antiviral cargo in proximity to the viral membrane.

2.7. Antiviral activity of CBNK-EVs against ZIKV in AG6 mice

To further confirm the protective effect of CBNK-EVs, AG6 mice (IFN receptor-knockout mice on a C57BL/6J background) were used for anti-ZIKV evaluation (Fig. 7a). We first determined the distribution of CBNK-EVs in AG6 mice and found that they mainly accumulated in the liver (Fig. 7b and c). An ex vivo image revealed CBNK-EV signals in the kidneys and spleen (Fig. 7e). Following intravenous administration, CBNK-EVs exhibited broad biodistribution, with robust signals observed in the liver, spleen, and kidneys at 4 h, which progressively declined by 8 h and were largely cleared by 24 h (Fig. S5a and S5b). The signal was detected in the brains of AG6 mice 4 h post-injection (Fig. 7d and f) and clearly detectable until 8 h time point (Fig. S5c). This indicated that

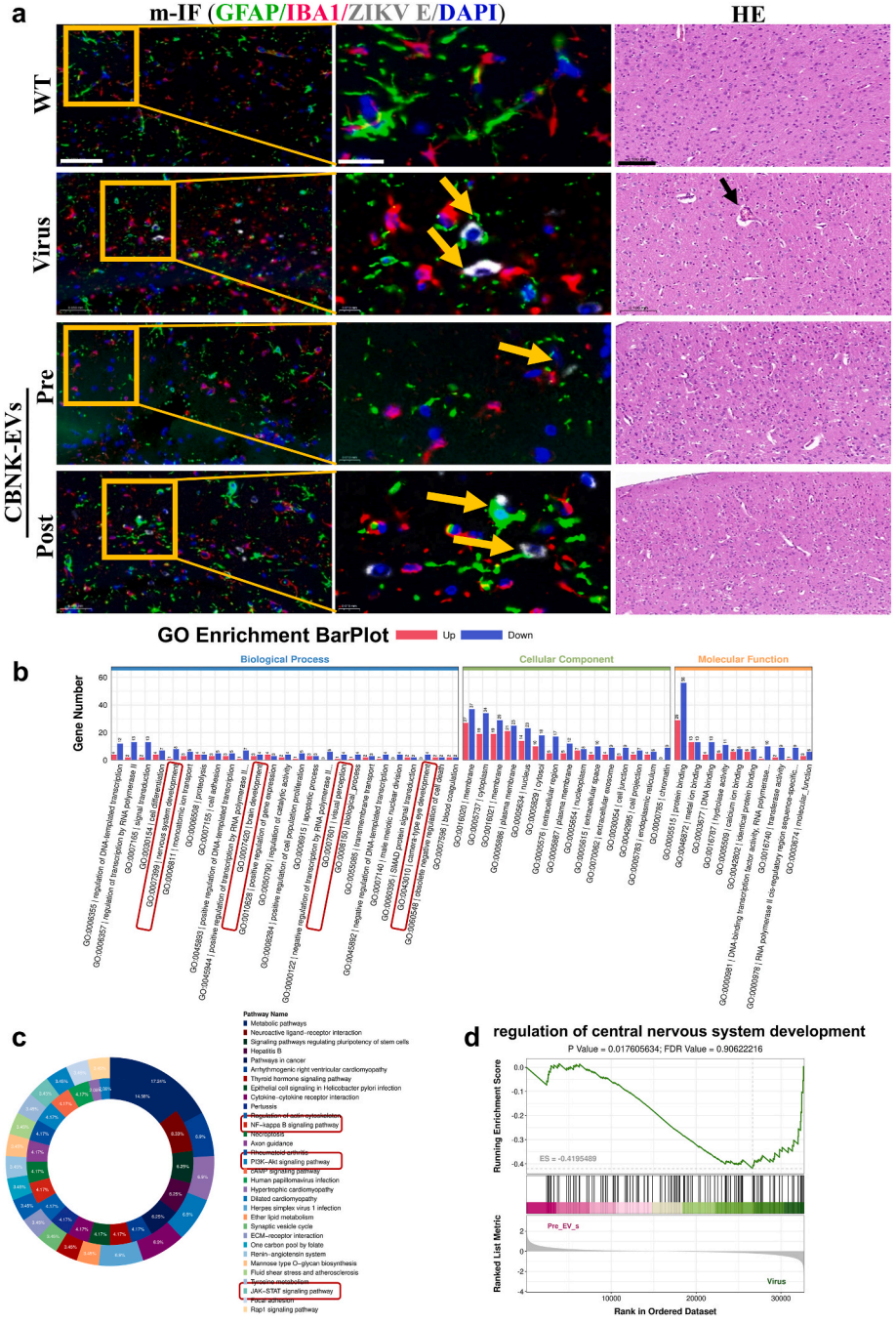

Fig. 8. CBNK-EVs reduce ZIKV infection and protect neuroglial cells from damage. **(a)** Multicolor immunofluorescence (scale bar: 50 μm) combined with H&E staining revealed the neuroprotective effects of CBNK-EVs in AG6 mice. In the magnified immunofluorescence panels (scale bar: 10 μm), yellow arrows indicate ZIKV E-positive signals. H&E staining of the cortical region (scale bar: 100 μm) revealed perivascular cuffing (black arrow) in virus group. **(b)** Compared to the Virus group, GO analysis revealed that CBNK-EV pre-treatment markedly attenuated the expression of genes associated with ZIKV induced neurodevelopmental impairment. **(c)** Compared to the Virus group, KEGG pathway analysis indicated a significant reduction in ZIKV-triggered activation of innate immune signaling and inflammatory cascades. **(d)** Compared to the Virus group, GSEA demonstrated a reversal of the aberrant expression profile for genes implicated in ZIKV-mediated central nervous system developmental disruption.

CBNK-EVs were effective accumulation in the central nervous system. Similar to peripheral organs, the intracerebral signal decreased markedly by 24 h (Fig. S5d and S5e). Unlike in fetuses, where ZIKV infection of neural progenitors causes developmental abnormalities, the virus in adults targets neurons and glial cells, triggering subsequent neuroinflammation [26]. Cryosections revealed that CBNK-EVs efficiently crossed the blood-brain barrier and were distributed throughout the hippocampus (Fig. 7g). CBNK-EV treatment significantly reduced abnormal behavioral scores and mortality in AG6 mice (Fig. 7h and i). Although a substantial fraction of CBNK-EVs were sequestered by the liver, both the pre- and post-treatment groups showed markedly attenuated ZIKV-induced viremia and curbed ZIKV RNA levels across the examined tissues (Fig. 7j). Similarly, multi-immunohistochemistry revealed that ZIKV primarily targeted astrocytes within the murine cerebral tissue and elicited pronounced perivascular cuffing (Fig. 8a). Pre-treatment with CBNK-EVs markedly reduced viral dissemination and preserved cerebral architecture (Fig. 8a). Consistent with the enteric tropism of ZIKV, CBNK-EVs attenuated viral propagation along the intestinal tract of AG6 mice (Fig. S5f). Acting as a viral-entry inhibitor, CBNK-EVs conferred comprehensive protection against ZIKV-induced cytopathology by restoring the aberrant transcriptional programs governing neurodevelopment (Fig. 8b). And CBNK-EVs decreased the activation of inflammatory signaling cascades, including NF-kB, JAK-STAT, and PI3K-AKT (Fig. 8c), thereby showed robust neuroprotection during central nervous system development (Fig. 8d).

3. Discussion

CBNK-EVs interacted with ZIKV particles and reduced viral infectivity. The interaction between ITGB2 and the ZIKV envelope (E) protein brings CBNK-EVs into proximity with the virus, thereby facilitating perforin-mediated disruption of the viral envelope, which functions similarly to viral entry inhibitors. CBNK-EVs played a role in suppressing ZIKV infection and replication. Importantly, as nanoscale vesicles, CBNK-EVs can effectively cross the placental and blood-brain barriers. This characteristic is crucial for preventing and treating CZS, and provides significant insights into the development of novel CBNK-EV-based therapeutics against ZIKV.

As a member of the family Flaviviridae, ZIKV is classified into two major genotypes: Asian and African. The Asian lineage has been identified as the primary causative agent of CZS and microcephaly [27]. The ZIKV genome encodes a polyprotein that is processed into three structural proteins (C, prM, and E) and seven non-structural proteins (NS1, NS2A, NS2B, NS3, NS4A, NS4B, and NS5). Among these, the E protein plays a critical role in host-cell binding, adhesion, and membrane fusion, making it a key target for antiviral strategies [28]. Since the last major outbreak of ZIKV in 2016, extensive research has advanced our understanding of ZIKV entry mechanisms, pathogenic traits, and immune evasion pathways [29], providing critical insights for the development of small-molecule inhibitors, peptide-based therapeutics [30], and vaccines [31]. Given the severe clinical manifestations associated with ZIKV infection, CBNK-EVs offer a novel perspective on the interactions between ZIKV and host cells, and demonstrate significant potential for future safe and effective anti-ZIKV therapies.

The antiviral potential of EVs derived from diverse sources has been highlighted. For instance, milk-or stem cell-derived EVs exert antiviral effects by delivering antiviral miRNAs or proteins to host cells [32]. The HIV-1 Nef protein reduces IFITM abundance in T cell-derived EVs, facilitating HIV reservoir establishment [33]. These findings underscore EVs as a novel communication platform for virus-host interactions. Notably, NK-EVs inherit functional cargo from the parental NK cells. Chung et al. reported that EVs from NK-92 cells exhibited anti-SARS-CoV-2 activity mediated by miRNAs, such as miR-27 and miR-491-5p [13]. However, the EV composition varies significantly across cellular origins. Compared with NK-92 cell-derived EVs, CBNK-EVs possess a more heterogeneous subtype profile and intercellular communication capacity [34], prompting us to focus on their role in combating flaviviral infections. Here, we demonstrate that CBNK-EVs neutralize ZIKV through direct virion capture and inactivation. These findings provide a rationale for the clinical application of CBNK-EVs, particularly via intravenous administration. The systemic delivery of CBNK-EVs would leverage their extracellular neutralization capacity to intercept circulating virions, thereby not only preventing initial cellular entry but also curbing the expansion of infection foci through interruption of cell-to-cell transmission [35]. While current data highlight their prophylactic efficacy and ability to block vertical transmission, the versatile biology of EVs suggests broader therapeutic utility. Future strategies may also employ CBNK-EVs as nanocarriers for delivering additional antiviral agents with distinct mechanisms [36], enabling a synergistic “cocktail” approach to treat established infections. Moreover, relative to neutralizing monoclonal antibodies (mAbs), CBNK-EVs present distinct advantages in addressing congenital Zika syndrome. Although mAbs exhibit potent neutralization and have achieved protective thresholds in non-human primates [37] or via viral vector delivery [38], CBNK-EVs possess unique functional attributes. First, CBNK-EVs inherently traverse the placental and blood–brain barriers—a capability notably absent in conventional mAbs, thus overcoming a key limitation in protecting fetal and neural tissues. Second, their antiviral action involves physical perforin-mediated disruption of the viral envelope, a destructive mechanism that contrasts with the epitope-targeted blockade typical of antibodies and may serve as a complementary strategy when viral mutations confer escape from mAb therapy. These characteristics position CBNK-EVs as a promising complementary modality to antibody-based interventions. It has also been proposed that engineered EVs exhibit strain-specific antiviral activities against different viral variants [39]. This underscores the necessity of employing diverse engineering strategies to further enhance therapeutic efficacy [40].Our data establish perforin-1 as a key mediator of this activity, as evidenced by TEM and a specific micrococcal nuclease digestion assay. Perforin-1 and granzyme B were encapsulated within the luminal compartment of CBNK-EVs. The formation of the fusion body is critical for the sudden increase in calcium ion concentration and subsequent perforin activation (Fig. 2h). While CBNK-EVs contain other antiviral factors such as IFITM1, which exhibits in vitro activity [41], it cannot account for the direct disruption of the viral envelope observed upon exposure to CBNK-EVs (Figs. 2i and 5c). It is noteworthy that perforin-1 possesses membrane-lytic activity against the ZIKV envelope [22]. Thus, the perforin-1-dependent envelope disruption represents a novel nanoscale mechanism, leading to the loss of virion integrity. Moreover, proteomic profiling revealed the abundant expression of ITGB2 on CBNK-EV surfaces, which bound to the ZIKV E protein and mediated membrane interactions. This interaction facilitates membrane fusion and enables perforin-mediated viral inactivation. Ca^{2+} is indispensable for EV biogenesis and release by donor cells [42]. However, the acidic luminal pH (≈5.0–6.0) of these EVs and markedly lower Ca^{2+} concentration relative to the extracellular milieu collectively maintain perforin in its monomeric, inactive state, thereby preserving EV integrity [43]. This homeostatic balance is abruptly disrupted when ITGB2 captures Zika virions, triggers their fusion with the EV membrane, and perturbs the weakly acidic microenvironment of the EV lumen. ITGB2-dependent docking drives an abrupt EV-virus membrane fusion event, resulting in a transient, spatially restricted Ca^{2+} surge that licenses perforin pore formation. Importantly, ITGB2, a receptor that is predominantly expressed in immune cells (especially monocytes), may serve as a novel integrin receptor for ZIKV entry. Monoclonal antibody blocking assays revealed that the high surface abundance of ITGB2 on CBNK-EVs was the principal determinant of their interaction with ZIKV. This binding and killing modality made CBNK-EVs viral entry inhibitors that effectively interrupt viral dissemination [44]. Although the integrins, ITGAV [45] and ITGB4 [23], have been implicated in ZIKV neurotropism, the role of ITGB2 in viral pathogenesis remains unexplored. ITGB2 is widely expressed in monocytes which played an important role

in inflammatory activation [46] and vertical transmission [5] during ZIKV infection.

NK cells have been reported to eliminate infected cells via cytolytic activity, exemplified by Nkp46 the recognition of ZIKV-induced endoplasmic reticulum stress markers in host cells [47]. Here, we provide a new perspective that CBNK-EVs engage ZIKV particles at the nanoscale, resulting in direct viral inactivation. Sequential administration of CBNK-EVs effectively shielded glial cells from ZIKV challenge, significantly reducing viremia and attenuating mortality in infected AG6 mice (Fig. 7h and i). Furthermore, CBNK-EVs demonstrated an unimpaired pregnancy outcome and a favorable maternal-fetal safety index in gravid mice (Fig. S3). Regarding the feasibility of clinical translation, assessing the production yield is essential. To achieve the high therapeutic doses required for in vivo experiments (up to 6×10^{12} particles/mL), we concentrated EVs from 1200 mL of conditioned medium. In our current laboratory method, we routinely recover approximately 1×10^{12} particles/mL EVs from 200 mL of CBNK cell culture supernatant. While such high-dose regimens are labor-intensive in a research setting, the scalability of EV production is rapidly advancing [48]. Future clinical manufacturing will likely necessitate the transition from conventional 2D cultures to 3D bioreactor systems [49], coupled with high-efficiency isolation methods such as tangential flow filtration [50]. These industrial optimizations are expected to significantly boost the yield and purity of CBNK-EVs, rendering high-concentration production both cost-effective and clinically accessible. Thus, our findings provide a translational foundation for both engineered vesicles and drug delivery-based antiviral strategies against ZIKV.

In summary, our work establishes CBNK-EVs as safe and effective nanotherapeutics against ZIKV infection. We found that ITGB2 binds to the ZIKV E protein, facilitating the inactivation of ZIKV by antiviral substances within CBNK-EVs. These findings provide a new strategy for engineering EV-based delivery systems to combat congenital Zika syndrome, especially to prevent vertical transmission and protect the fetus.

4. Materials and methods

4.1. Acquisition and isolation of CBNKs and CBNK-EVs

This study was reviewed and approved by the Ethics Committee of the Tenth Affiliated Hospital, Southern Medical University (MCSC2025-002-1). Under a sequential MACS strategy for untouched NK cell isolation, PBMCs are first subjected to negative selection using the human NK Cell Isolation Kit (Miltenyi Biotec, cat#130-092-657), which depletes $CD3^+$ T cells and other non-NK lineages; the resulting enriched flow-through is then immediately used for positive selection via incubation with human CD56 Microbeads (Miltenyi Biotec, cat#130-050-401), followed by a final magnetic separation to obtain a highly pure population of $CD3^-CD56^+$ NK cells. Freshly isolated NK cells were seeded at an initial density of $0.5–1.0 \times 10^6$ cells/mL in serum-free NK cell-specific medium (Lonza NKMACO™ Medium, cat#BE001NC), supplemented with 500IU/mL recombinant human IL-2 (PeproTech, cat#200–02) and 10 ng/mL recombinant human IL-15 (PeproTech, cat#200–15). The cells were maintained in a humidified incubator at 37 °C with 5 % CO_2. The culture was fed every 2–3 days by replacing half of the spent medium with fresh, pre-warmed complete medium containing the same concentrations of cytokines, ensuring cell density was maintained between 0.5 and 2.0×10^6 cells/mL.

All supernatants were collected for EVs isolation through sequential ultracentrifugation [51]. Briefly, supernatants were first filtered through a 0.22 μm membrane to remove large cellular debris, followed using centrifugation at 12,000g for 30 min to eliminate large protein aggregates or vesicles. And then, the EVs were pelleted using ultracentrifugation at 110,000g for 70 min. Finally, CBNK-EVs were diluted with exosome-free phosphate-buffered saline (PBS) to the desired concentration and stored at −80 °C for subsequently experiments.

4.2. Characterization of CBNK-EVs

The purified CBNK-EVs were characterized using standardized methodologies to confirm their identity and quality. Protein concentration was quantified via the BCA assay, while nanoparticle tracking analysis (NTA) determined EV particle concentration and size distribution. Transmission electron microscopy (TEM) revealed the characteristic cup-shaped morphology of EVs. Furthermore, Western blot analysis confirmed the presence of canonical EV markers, including Tsg101 (Peoteintech, cat#67381), CD9 (Peoteintech, cat#20597), CD81 (Peoteintech, cat#66866), and ALIX (Peoteintech, cat#12422), ensuring the enrichment of authentic extracellular vesicles. Additionally, the absence of the negative marker Calnexin (Abcam, cat#ab133615) was verified to confirm the purity of the CBNK-EVs.

4.3. Cytotoxicity evaluation of CBNK-EVs

To assess the cytotoxicity of CBNK-EVs, Vero-E6 and BHK-21 cells were seeded in 96-well plates at a density of 2×10^4 cells/mL and allowed to adhere overnight. Serial dilutions of CBNK-EVs (ranging from 2×10^{12} particles/mL to 3.125×10^{10} particles/mL, 7 concentration gradients) were co-incubated with the adherent cells. After 48 h of treatment, cell viability was determined using the CCK-8 assay by measuring absorbance at 450 nm.

To define a safe and effective therapeutic regimen, a dose-escalation safety study was conducted in pregnant BALB/c mice ($n = 6$ per group). Mice were administered intravenous injections of CBNK-EVs at three increasing concentrations (6×10^{11}, 2×10^{12}, and 6×10^{12} particles/mL, every other day) or an equal volume of PBS for 14 days. Maternal body weight, fetal development, ALT and creatinine, and tissue histopathology were monitored to assess the safety of CBNK-EVs.

4.4. Evaluation of antiviral activity in vitro

ZIKV (z16006 and SZ01) were maintained in our laboratory under biosafety level 2 (BSL2) and viral stock was quantified using the TCID50 endpoint dilution assay [16]. Vero E6, BHK21, 293T and HTR-8/Svneo cells were purchased from ATCC. The ZIKV strain z16006 was used in cell-based experiments unless otherwise stated. To systematically investigate the antiviral mechanisms of CBNK-EVs, we used four distinct treatment regimens by varying the temporal sequence of EV administration relative to the viral infection. Generally, fresh medium was changed after 1 h of viral adsorption. For the full stage assay, CBNK-EVs were premixed with the viral suspension prior to target cell infection, with subsequent maintenance in EV-containing post-infection medium. This assay was used to determine the preliminary activity of EVs against ZIKV and DENV. For the co-culture approach, CBNK-EVs were premixed with the viral suspension prior to target cell infection, with subsequent maintenance in EV-free medium post-infection. For cell pre-treatment, target cells were incubated with CBNK-EVs for 2 h before viral challenge and EVs were removed during infection. For viral pretreatment, CBNK-EVs were incubated with viral particles for 2 h prior to target cell exposure. The antiviral activities of recombinant human perforin-1 (USCN, cat#RPB317H01) and recombinant human granzyme B (USCN, cat#RPB600H01) were evaluated using a co-culture approach. Finally, the samples were collected for WB or RT-qPCR. Anti-ZIKV E (Gene Tex, cat#GTX133314), anti-ZIKV NS5 (Gene Tex, cat#GTX133328), anti-GAPDH (Gene Tex, cat#GTX100118), and anti-DENV NS5 (Gene Tex, cat#GTX629446) were used in WB. The primers used for RT-qPCR are listed in Supplementary Table 1. Bulk RNA-seq was performed on HTR-8/Svneo cells exposed to CBNK-EVs, ZIKV, or their combination, to dissect the transcriptional landscape underlying CBNK-EV-mediated protection against ZIKV infection (supported by Genedenovo, China).

4.5. CBNK-EVs uptake assay

For fluorescent labeling of CBNK-EVs, isolated vesicles were incubated with DID (Thermo Fisher Scientific, cat#V22887), followed by the removal of excess dye using size-exclusion chromatography (Enzekangtai, cat#ES9016). Vero-E6 cells were plated in confocal dishes (Corning, cat#430660) and allowed to adhere for 12 h. DID-labeled CBNK-EVs were then added to the cells and incubated for an additional 12 h at 37 °C. After fixation, cells were stained for cytoskeletal markers and nuclei (DAPI) prior to imaging with laser scanning confocal microscopy (Zeiss, LSM900).

4.6. Distribution of CBNK-EVs in mice

Pregnant BALB/c mice on gestational day 10 were randomly divided into two groups (n = 6 per group). The treatment group received intravenous injection of DID-labeled CBNK-EVs (6×10^{12} particles/mL), while control animals were administered equal-volume PBS. Whole-body fluorescence imaging was performed at 4, 8, and 24 h post-injection using the IVIS Lumina K Series III imaging system (PerkinElmer), with quantitative analysis of radiant efficiency ([p/s/cm^2/sr]/[μW/cm^2]) conducted using Living Image 4.4 software. For organ-specific distribution assessment, mice were euthanized via a pentobarbital sodium overdose, followed by ex vivo imaging of dissected uterine tissues and fetuses at indicated time points to determine the regional fluorescence intensity. A similar protocol was employed to assess the distribution of CBNK-EVs in AG6 mice. The brains of AG6 mice were harvested, snap-frozen in liquid nitrogen, and processed into cryosections for direct visualization of the distribution of CBNK-EVs within the brain. Animal experiments were approved by the Animal Ethics Committee of Southern Medical University (IACUC-AWEC-202511004).

4.7. Immunofluorescence (IF) assay

For IF analysis, cells were washed with PBS and fixed with 4 % paraformaldehyde on ice for 15 min. Permeabilization was performed using 0.1 % Triton X-100 for 10 min at 25 °C, followed by blocking with 5 % goat serum for 1 h to minimize non-specific binding. Cells were then incubated overnight at 4 °C with primary antibodies targeting ZIKV E protein (Gene Tex, cat# GTX133314), β-actin (Fude Biotech, cat# FD0060), GFAP (Servicebio, cat# GB12090), IBA1 (Servicebio, cat# GB12015), Nestin (Cell Signaling Technology, cat#33475), Claudin1 (Cohesionbio, cat# CPA2349). After washing with PBS, the samples were stained with the appropriate fluorophore-conjugated secondary antibodies (1:500 dilution) for 1 h at room temperature in the dark. Nuclei were counterstained with DAPI. For immunofluorescence quantification, positive cells were manually counted in each microscopic field by two blinded, independent observers. Their counts were averaged to generate a single value per field. A minimum of three random fields were analyzed per biological sample to ensure representative sampling across all experimental groups. Statistical comparisons among the multiple groups were performed using a one-way analysis of variance (ANOVA) followed by an appropriate post-hoc test for detailed group-wise comparisons. Data are presented as mean ± standard deviation, with a p-value <0.05 considered statistically significant.

4.8. Transmission electron microscope assay (TEM)

The shape of Zika virus and EVs were characterized by transmission electron microscope (TEM). Briefly, samples were fixed by 1 % PFA and placed on a carbon-coated copper grid. After incubation for 5 min at room temperature, the grid was stained negatively with 3 % phosphotungstic acid (pH = 7.0) for 2 min. Then, samples were imaged by TEM (Hitachi, HT7800).

4.9. Micrococcal nuclease digestion assay

To quantify intact ZIKV virions and evaluate their disruption by EVs, viral RNA levels were measured by RT-qPCR. Briefly, ZIKV stock (MOI = 1) was incubated with EVs, 1 % Triton X-100 (positive control), or culture medium (negative control) at 37 °C for 1 h. Each sample was then treated with 20 μl of micrococcal nuclease at 37 °C for 30 min to degrade unprotected RNA. The reaction was terminated by adding 10 mM EGTA. Protected viral RNA was extracted using the Viral RNA Kit (Takara, cat#9766), and quantified by real-time PCR.

4.10. Plaque reduction assay

Vero E6 cells were seeded in 12-well plates at a density of 2×10^5 cells per well and cultured overnight until full adherence was achieved. The culture medium was then discarded, and each well was washed twice with 1 mL of PBS. Following viral infection (MOI = 1), the plates were incubated at 37 °C with 5 % CO_2 for 1 h [52]. After removing the viral inoculum and washing with PBS, 2 mL of DMEM containing 1.2 % methylcellulose, 2 % FBS, and 1 % double antibiotics was added to each well. The cells were further cultured for 4–5 days. Upon observation of significant cytopathic effect, the overlay medium was discarded, and the cells were washed once with PBS. Subsequently, 1 mL of 1 % crystal violet in 4 % paraformaldehyde was added to each well for fixation and staining at room temperature for 60 min. The crystal violet solution was collected for reuse, and residual dye was gently rinsed off with PBS.

4.11. Plasmid and siRNA transfection

For plasmid transfection, HEK-293T cells were seeded in 12-well plates at a density of 2×10^5 cells per well. The following day, cells were transfected with plasmids encoding ITGAX (Flag-tag, cat#P5898) and ITGB2 (HA-tag, cat#P6024) were purchased from Miaoling Biotechnology and transfected with polyjet reagent (SigmaGen, cat# SL100688) according to the manufacturer's instructions [53]. Cells were harvested 48 h post-transfection for analysis.

For siRNA transfection, suspension NK cells were prepared at a density of 5×10^6 to 1×10^7 cells/mL in Opti-MEM. Perforin 1 siRNA (sc-42592, Santa Cruz Biotechnology) was delivered into the cells using the ProteanFect transfection kit (PT02-0010A, NanoPortal Biotech), following the manufacturer's protocol designated for primary cells. The final siRNA concentration was 1 μM for each individual siRNA (siRNA1, siRNA2, siRNA3). The cell-transfection complex mixture was incubated at 37 °C for 15–30 min. After termination of the reaction and washing, the transfected NK cells were cultured for 48 h prior to further experimentation. The dose-dependent knockdown efficiency of siRNA3 targeting perforin1 was further confirmed (0.25 μM, 0.5 μM, and 1 μM).

4.12. Time-course incubation experiment

Vero-E6 cells in the logarithmic growth phase were seeded in 12-well plates at 1×10^5 cells/well. EVs were premixed with ZIKV (MOI = 1) and incubated at room temperature for 5, 10, 20 or 30 min before being added to the cells. After 1 h of adsorption at 37 °C, the inoculum was removed, and cells were further cultured for 48 h prior to protein collection.

4.13. ZIKV infection in mice

Pregnant BALB/c mice received an intraperitoneal injection of anti-IFNAR monoclonal antibody (BioXcell, cat#BE0241) one day before virus challenge to block innate immune signaling. On the following day, the dams were intravenously (i.v.) inoculated with 4×10^5 TCID50 of ZIKV. In the treatment group, CBNK-EVs (6×10^{12} particles/mL, 200 μl each) were administered intravenously 4 h prior to virus challenge. Heat-inactivated CBNK-EVs (CBNK-HI-EVs) at the same concentration

served as the negative control.

For AG6 mice, a Ifngr 1/Ifnar 1-KO [−/−] in C57BL/6J, were obtained from Cyagen Biosciences (cat#C001268) and used to evaluate the antiviral efficacy of EVs in vivo as another ZIKV-susceptible model. Mice (6–8 weeks) were divided into four groups: Vehicle control, ZIKV-only, Pre-treat EVs and Post-treat EVs. All groups except Vehicle received an intraperitoneal injection of 2×10^4 TCID50 ZIKV (200 μl) on day 0. The Pre-treat EVs group was administered CBNK-EVs (6×10^{12} particles/mL, 200 μl, i.v.) on two consecutive days prior to viral challenge (days −2 and −1). The Post-treat EVs group received the same dose of CBNK-EVs, with the first injection at 1 h post-infection, followed by daily administration for six days. On day 9, mice were euthanized by cervical dislocation, and serum/tissues (heart, liver, spleen, lung, kidney, brain, and colon) were harvested for histopathological analysis, protein extraction, and RNA detection. Brain samples of ZIKV-only and Pre-treat EVs were collected for RNA-sequencing.

To evaluate clinical disease, mice were assigned and scored as described before [54]: A) no disease, 0; B) hindlimb weakness or disrupted righting reflex, 1; C) partial hindlimb paralysis or toe knuckling, 2; D) complete paralysis of one hindlimb, 3; E) complete paralysis of both hindlimbs, 4; F) complete paralysis of all four limbs, 5 or G) moribund or dead, 6. Mice with a disease score of F or G were euthanized.

4.14. RNA-sequencing

For the in vitro study, HTR-8/Svneo cells were divided into three groups (n = 3 for each): uninfected (WT), ZIKV-infected (Virus), and ZIKV-infected treated with CBNK-EVs (CBNK-EVs). Cells were harvested at 24 h post-infection. For the in vivo study, brain tissues were collected from AG6 mice at the experimental endpoint. We compared transcriptomic profiles between the ZIKV-infected group and the pre-treatment CBNK-EVs group (n = 3). Total RNA was extracted from samples using TRIzol reagent, and its quality was rigorously assessed. Following poly(A) + RNA purification with Dynabeads Oligo(dT), the mRNA was fragmented and reverse-transcribed into cDNA. Second-strand synthesis was performed incorporating dUTP for strand marking. The resulting cDNA fragments underwent end-repair, A-tailing, and adapter ligation. After size selection, the libraries were treated with UDG enzyme and amplified via PCR. Final library quality was confirmed, and paired-end 150 bp sequencing was performed on an Illumina Novaseq 6000 platform (LC-Bio Technologies).

4.15. Bioinformatics and functional enrichment analysis

The raw sequencing data underwent quality control and adapter trimming using the fastp software (https://github.com/OpenGene/fastp). High-quality reads were then aligned to the *Homo sapiens* GRCh38 reference genome using HISAT2 (https://ccb.jhu.edu/software/hisat2). Transcript assembly and gene expression quantification (in FPKM) were performed with StringTie (https://ccb.jhu.edu/software/stringtie). Differential expression analysis was conducted using the edgeR package in R (https://bioconductor.org/packages/release/bioc/html/edgeR.html), applying thresholds of a fold change >2 or <0.5 and a p-value <0.05. Finally, functional enrichment analysis for Gene Ontology (GO) terms and Kyoto Encyclopedia of Genes and Genomes (KEGG) pathways was performed on the differentially expressed genes using the clusterProfiler R package.

4.16. Proteomics analysis

Proteomics analysis of CBNK-EVs was supported by Wayen Biotechnologies Co., Ltd. (China). For the NK cell related proteins screening, human protein atlas (HPA) database was used for identification and analysis.

4.17. Enzyme-linked immunosorbent assay (ELISA)

Hepatic and renal function in pregnant mice was assessed by measuring serum levels of alanine aminotransferase (Meimian, cat#MM44625M1) and creatinine (Meimian, cat#MM0693M1). In parallel, the absolute contents of perforin-1 (KeyGen, cat#KGC1168) and granzyme B (Meimian, cat#MM-0434H2) within CBNK-EVs were quantified by ELISA.

ZIKV infection was quantified using a cell-based immunodetection assay for viral E protein [18]. Vero-E6 cells infected with ZIKV for 4 days were fixed with 4 % paraformaldehyde and permeabilized with methanol. Fixed cells were incubated with anti-ZIKV E antibody (Gene Tex, cat#GTX133314), followed by an HRP-conjugated secondary antibody (Cell Signaling Technology, cat#7074S). Signal was developed with TMB substrate, the absorbance was measured at 450 nm.

4.18. Docking analysis

Amino acid sequences of E protein and ITGB2 protein were retrieved from the UniProt database (www.uniprot.org/). Molecular docking of E protein with the ligand-binding region of ITGB2 (1- 460aa) was performed. E protein exhibited an antiparallel dimer structure, and the coloring of its three domains was consistent with previous reports [55]. The structure of E protein dimer in complex with ITGB2 was predicted using AlphaFold3.

4.19. Co-immunoprecipitation

HEK-293 T cells were seeded in dishes at 1.5×10^5 cells/ml 24 h before the Flag-ITGAX and HA-ITGB2 plasmids transfection. After 48 h, the cells were infected with ZIKV at proper titer. Protein was collected after another 48 h and the lysates were normalized to 3 μg/μl with IP buffer, 300 μl (equivalent to 900 μg total protein) was used for each immunoprecipitation reaction. For antibody coupling, 2 μg of the anti-Flag antibody (Sigma-Aldrich, cat#F1804), anti-HA antibody (Beyotime, cat#AH158), or rabbit control IgG (Beyotime, cat#A7016) was incubated with protein beads (Beyotime, cat# P2108) for 12 h at 4 °C. The normalized lysate was then mixed with the antibody-coupled beads and incubated overnight at 4 °C, followed by three times wash, protein linked on beads was finally denatured in sample buffer at 95 °C for 10 min and Western blot assay was performed subsequently.

4.20. Zika virus infection in pups

Pregnant mice were injected with IFNAR-1 blocking antibody at a dose of 10 mg/kg (Leinco Technologies, cat#1021L220) and then exposed to 4×10^5 TCID50 of ZIKV to promote ZIKV infection in the pups as described before [56]. CBNK-EVs (6×10^{12} p/ml, 200 μl per mouse) were administered via tail vein injection for three consecutive days. After seven days, mice were sacrificed and materials were collected to evaluate the protective effects of CBNK-EVs on fetal mice.

4.21. Histopathological and immunofluorescence analysis

The tissue slides after deparaffinization were stained with hematoxylin and eosin to observe structural characteristics. For immunofluorescence staining, the deparaffinized sections were put in microwave oven to repair antigen. Slides were permeated in 0.1 % tritonx-100 and then incubated with appropriate primary antibodies at 4 °C overnight and then the multicolor fluorescent labeling kit (HISTOV, cat#DFT67100) was used to perform iterative antigen retrieval and labeling with different primary antibodies, followed by imaging under a fluorescence scanning microscope (3DHISTECH, Pannoramic MIDI II).

4.22. Statistical analysis

All data examined are expressed as mean ± SEM. Statistical analyses of the data were performed using Graphpad Prism (Version 8.0). The comparisons between groups were analyzed using one-way ANOVA. $P < 0.05$ was considered to have a significant difference. Semi-quantitative analysis was performed by Image J.

CRediT authorship contribution statement

Chen Cheng: Validation, Investigation. **Ru Li:** Supervision, Funding acquisition. **Tianwang Guan:** Methodology, Investigation, Data curation. **Haowei Li:** Writing – original draft, Methodology, Investigation, Funding acquisition. **Luping Cheng:** Validation, Methodology. **Min Zou:** Writing – review & editing, Supervision, Funding acquisition. **Shuwen Liu:** Writing – review & editing, Validation, Methodology. **Caiwen Ou:** Guang Li, Methodology, Investigation.

Ethics approval and consent to participate

The use of cord blood for NK cell isolation in this study was approved by the Ethics Committee of The Tenth Affiliated Hospital, Southern Medical University (Approval number: MCSC2025-002-1). All animal procedures were conducted under a protocol approved by the Animal Ethics Committee of Southern Medical University (Approval number: IACUC-AWEC-202511004).

Declaration of competing interest

The authors declare that they have no known competing financial interests or personal relationships that could have appeared to influence the work reported in this paper.

Acknowledgments

This work was supported by the China Postdoctoral Science Foundation (2025M771982 to C.C.), Guangdong Basic and Applied Basic Research Foundation (2024A1515110217 to C.C. and 2023B1515130005 to CW.O.), Key-Area Research and Development Program of Guangdong Province (2023B1111050008 to SW.L.), National Natural Science Foundation of China (32371428 to CW.O.) and Dongguan Social Development Science and Technology Project (No. 20231800932472).

Appendix B. Supplementary data

Supplementary data to this article can be found online at https://doi.org/10.1016/j.bioactmat.2026.01.030.

Data availability

Data will be made available on request.

References

[1] P. Brasil, J.P. Pereira Jr., M.E. Moreira, R.M. Ribeiro Nogueira, L. Damasceno, M. Wakimoto, et al., Zika Virus Infection in Pregnant Women in Rio de Janeiro, N. Engl. J. Med. 24 (2016) 2321–2344, https://doi.org/10.1056/NEJMoa1602412.
[2] D. Baud, D.J. Gubler, B. Schaub, M.C. Lanteri, D. Musso, An update on Zika virus infection, Lancet 390 (2017) 2099–2109, https://doi.org/10.1016/S0140-6736(17)31450-2.
[3] M.R. Koenig, A.M. Mitzey, X. Zeng, L. Reyes, H.A. Simmons, T.K. Morgan, et al., Vertical transmission of african-lineage Zika virus through the fetal membranes in a rhesus macaque (Macaca mulatta) model, PLoS Pathog. 8 (2023) e1011274, https://doi.org/10.1371/journal.ppat.1011274.
[4] R.T. Michita, L.B. Tran, S.J. Bark, D. Kumar, S.A. Toner, J. Jose, et al., Zika virus NS1 drives tunneling nanotube formation for mitochondrial transfer and stealth transmission in trophoblasts, Nat. Commun. 16 (2025) 1803, https://doi.org/10.1038/s41467-025-56270-6.
[5] M. Abdelbasset, W.A.A. Saron, D. Ma, A.P.S. Rathore, T. Kozaki, C. Zhong, et al., Differential contributions of fetal mononuclear phagocytes to Zika virus neuroinvasion versus neuroprotection during congenital infection, Cell 26 (2024) 7511–7532.e20, https://doi.org/10.1016/j.cell.2024.11.032.
[6] N. Shahrizaila, H.C. Lehmann, S. Kuwabara, Guillain-Barré syndrome, Lancet. 397 (2021) 1214–1228, https://doi.org/10.1016/S0140-6736(21)00517-1.
[7] A. Wilder-Smith, A. Durbin, Promising efforts to develop an mRNA vaccine against Zika, Lancet Infect. Dis. 5 (2023) 520–522, https://doi.org/10.1016/S1473-3099(23)00196-2.
[8] C. He, C. Hu, W.Z. He, Y.C. Sun, Y. Jiang, L. Liu, et al., Macrophage-derived extracellular vesicles regulate skeletal stem/progenitor cell lineage fate and bone deterioration in obesity, Bioact. Mater. 36 (2024) 508–523, https://doi.org/10.1016/j.bioactmat.2024.06.035.
[9] J. Johnson, S.Q.K. Law, M. Shojaee, A.S. Hall, S. Bhuiyan, M.B.L. Lim, et al., First-in-human clinical trial of allogeneic, platelet-derived extracellular vesicles as a potential therapeutic for delayed wound healing, J. Extracell. Vesicles 7 (2023) e12332, https://doi.org/10.1002/jev2.12332.
[10] Z. Chu, Q. Huang, K. Ma, X. Liu, W. Zhang, S. Cui, et al., Novel neutrophil extracellular trap-related mechanisms in diabetic wounds inspire a promising treatment strategy with hypoxia-challenged small extracellular vesicles, Bioact. Mater. 27 (2023) 257–270, https://doi.org/10.1016/j.bioactmat.2023.04.007.
[11] S.G. Dosil, S. Lopez-Cobo, A. Rodriguez-Galan, I. Fernandez-Delgado, M. Ramirez-Huesca, Milan-Rois, et al., Natural killer (NK) cell-derived extracellular-vesicle shuttled microRNAs control T cell responses, eLife 11 (2022) e76319, https://doi.org/10.7554/eLife.76319.
[12] C.H. Wu, J. Li, L. Li, J. Sun, M. Fabbri, A.S. Wayne, et al., Extracellular vesicles derived from natural killer cells use multiple cytotoxic proteins and killing mechanisms to target cancer cells, J. Extracell. Vesicles 8 (2019) 1588538, https://doi.org/10.1080/20013078.2019.1588538.
[13] S.A. Lim, N. Ho, S. Chen, E.J. Chung, Natural killer cell-derived extracellular vesicles as potential anti-viral nanomaterials, Adv Healthc Mater 19 (2024) e2304186, https://doi.org/10.1002/adhm.202304186.
[14] F. Fang, S. Xie, M. Chen, Y. Li, J. Yue, J. Ma, et al., Advances in NK cell production, Cell. Mol. Immunol. 4 (2022) 460–481, https://doi.org/10.1038/s41423-021-00768-8.
[15] K.W. Witwer, D.C. Goberdhan, L. O'Driscoll, S. Rome, S. Sahoo, L. Zheng, et al., Updating MISEV: evolving the minimal requirements for studies of extracellular vesicles, J. Extracell. Vesicles 10 (2021) e12182, https://doi.org/10.1002/jev2.12182.
[16] X. Qian, H.N. Nguyen, M.M. Song, C. Hadiono, S.C. Ogden, C. Hammack, et al., Brain-Region-Specific organoids using mini-bioreactors for modeling ZIKV exposure, Cell 5 (2016) 1238–1254, https://doi.org/10.1016/j.cell.2016.04.032.
[17] V.R. Yenuganti, S. Afroz, R.A. Khan, C. Bharadwaj, D.K. Nabariya, N. Nayak, et al., Milk exosomes elicit a potent anti-viral activity against dengue virus, J. Nanobiotechnol. 20 (2022) 317, https://doi.org/10.1186/s12951-022-01496-5.
[18] Y. Feng, Y. Yang, S. Zou, S. Qiu, H. Yang, Y. Hu, et al., Identification of alpha-linolenic acid as a broad-spectrum antiviral against zika, dengue, herpes simplex, influenza virus and SARS-CoV-2 infection, Antivir. Res. 216 (2023) 105666, https://doi.org/10.1016/j.antiviral.2023.105666.
[19] F. Tomatis, S. Rosa, S. Simões, M. Barão, C. Jesus, J. Novo, et al., Engineering extracellular vesicles to transiently permeabilize the blood-brain barrier, J. Nanobiotechnol. 1 (2024) 747, https://doi.org/10.1186/s03019w.
[20] A.A. Sow, P. Jamadagni, P. Scaturro, S.A. Patten, L. Chatel-Chaix, A zebrafish-based in vivo model of Zika virus infection unveils alterations of the glutamatergic neuronal development and NS4A as a key viral determinant of neuropathogenesis, PLoS Pathog. 20 (2024) e1012756, https://doi.org/10.1371/journal.ppat.1012756.
[21] J. Li, C. Zhu, Y. Meng, L. Zhang, C. Liu, Y. Qin, M. Chen, Zika virus inhibits cell death by inhibiting the expression of NLRP3 and A20, J. Virol. 3 (2025) e0198024, https://doi.org/10.1128/jvi.01980-24.
[22] M.E. Ivanova, N. Lukoyanova, S. Malhotra, M. Topf, J.A. Trapani, I. Voskoboinik, et al., The pore conformation of lymphocyte perforin, Sci. Adv. 6 (2022), https://doi.org/10.1126/sciadv.abk3147 eabk3147.
[23] H. Cong, J. Wang, N. Du, L. Song, R. Wang, Y. Yang, et al., ITGB4/CD104 mediates zika virus attachment and infection, Nat. Commun. 1 (2024) 10729, https://doi.org/10.1038/s41467-024-54683-3.
[24] S. Ramos da Silva, F. Cheng, I.C. Huang, J.U. Jung, S.J. Gao, Efficiencies and kinetics of infection in different cell types/lines by African and Asian strains of Zika virus, J. Med. Virol. 2 (2019) 179–189, https://doi.org/10.1002/jmv.25329.
[25] L. El-Shennawy, A.D. Hoffmann, N.K. Dashzeveg, K.M. McAndrews, A. R. Demonbreun, M.G. Ison, et al., Circulating ACE2-expressing extracellular vesicles block broad strains of SARS-CoV-2, Nat. Commun. 1 (2022) 405, https://doi.org/10.1038/s41467-022-28155-5.
[26] M.R. Lourenço, R.R. Christoff, T. Rabello, et al., Postnatal Zika virus infection increases seizure susceptibility and disrupts cortical organization and GABAergic interneuron positioning in mice, Neuroscience 2 (2025) 125–132, https://doi.org/10.1016/j.neuroscience.2025.02.016.
[27] C. Lefèvre, G.M. Cook, A.M. Dinan, S. Torii, H. Stewart, G. Gibbons, et al., Zika viruses encode 5' upstream open reading frames affecting infection of human brain cells, Nat. Commun. 1 (2024) 8822, https://doi.org/10.1038/s41467-024-53103-w.
[28] P. Tebas, C.C. Roberts, K. Muthumani, E.L. Reuschel, S.B. Kudchodkar, F.I. Zaidi, et al., Safety and immunogenicity of an anti-zika virus DNA vaccine, N. Engl. J. Med. 12 (2021) e35, https://doi.org/10.1056/NEJMoa2028120.

[29] M.I. Giraldo, M. Gonzalez-Orozco, R. Rajsbaum, Pathogenesis of zika virus infection, Annu. Rev. Pathol. 18 (2023) 181–203, https://doi.org/10.1146/annurev-pathmechdis-031521-034010.
[30] Y. Yu, Y.Q. Deng, P. Zou, Q. Wang, Y. Dai, F. Yu, et al., A peptide-based viral inactivator inhibits Zika virus infection in pregnant mice and fetuses, Nat. Commun. 8 (2017) 15672, https://doi.org/10.1038/ncomms15672.
[31] P. Abbink, K.E. Stephenson, D.H. Barouch, Zika virus vaccines, Nat. Rev. Microbiol. 10 (2018) 594–600, https://doi.org/10.1038/s41579-018-0038-8.
[32] M. Yuan, X. Tian, W. Ma, R. Zhang, X. Zou, Y. Jin, et al., miRNA-431-5p enriched in EVs derived from IFN-β stimulated MSCs potently inhibited ZIKV through CD95 downregulation, Stem Cell Res. Ther. 1 (2024) 435–448, https://doi.org/10.1186/s13287-024-03818-w.
[33] M.E. da Silva-Januário, C.S. da Costa, L.A. Tavares, A.K. Oliveira, Y.C. Januário, A. N. de Carvalho, et al., HIV-1 nef changes the proteome of T cells extracellular vesicles depleting IFITMs and other antiviral factors, Mol. Cell. Proteomics 12 (2023) 100676, https://doi.org/10.1016/j.mcpro.2023.100676.
[34] M. Li, H. Huang, X. Wei, H. Li, J. Li, B. Xie, et al., Clinical investigation on nebulized human umbilical cord MSC-derived extracellular vesicles for pulmonary fibrosis treatment, Signal Transduct. Targeted Ther. 19 (2025) 179, https://doi.org/10.1038/s41392-025-02115-3.
[35] L. Lu, S. Su, H. Yang, S. Jiang, Antivirals with common targets against highly pathogenic viruses, Cell 6 (2021) 1604–1620, https://doi.org/10.1016/j.cell.2021.02.013.
[36] X. Cheng, B.S. Henick, K. Cheng, Anticancer therapy targeting cancer-derived extracellular vesicles, ACS Nano 9 (2024) 6748–6765, https://doi.org/10.1021/acsnano.3c06462.
[37] J.P. Nkolola, D. Hope, R. Guan, A. Colarusso, M. Aid, D. Weiss, et al., Protective threshold of a potent neutralizing Zika virus monoclonal antibody in rhesus macaques, J. Virol. 12 (2024) e0142924, https://doi.org/10.1128/jvi.01429-24.
[38] H.Y. Ko, Y.Y. Li, Y. Simanjuntak, H.P. Yu, M.T. Chiang, et al., AAV-mediated delivery of a broadly neutralizing anti-flavivirus antibody protects against dengue and Zika viruses in a mouse model, Mol. Ther. 12 (2025) 6415–6430, https://doi.org/10.1016/j.ymthe.2025.09.007.
[39] M. Schürz, I. Pagani, E. Klinglmayr, H. Melo Benirschke, Mayora Neto, et al., Quantitative characterisation of extracellular vesicles designed to decoy or compete with SARS-CoV-2 reveals differential mode of action across variants of concern and highlights the diversity of Omicron, Cell Commun. Signal. 23 (2025) 323, https://doi.org/10.1186/s12964-025-02223-x.
[40] S. Liu, M. Liu, Z. Wang, S. Hu, K. Zhang, C. Lu, et al., Engineering bispecific exosome activators of T cells to target immune checkpoint inhibitor-resistant metastatic melanoma, Nat. Biotechnol. 5 (2026), https://doi.org/10.1038/s41587-025-02890-8.
[41] A.M. Chmielewska, M. Gómez-Herranz, P. Gach, et al., The role of IFITM proteins in tick-borne encephalitis virus infection, J. Virol. 1 (2022) e0113021, https://doi.org/10.1128/JVI.01130-21.
[42] L.A. Ambattu, S. Ramesan, C. Dekiwadia, E. Hanssen, H. Li, L.Y. Yeo, High frequency acoustic cell stimulation promotes exosome generation regulated by a calcium-dependent mechanism, Commun. Biol. 1 (2020) 553, https://doi.org/10.1038/s42003-020-01289-2.
[43] C. Leung, A.W. Hodel, A.J. Brennan, N. Lukoyanova, S. Tran, C.M. House, et al., Real-time visualization of perforin nanopore assembly, Nat. Nanotechnol. 5 (2017) 467–473, https://doi.org/10.1038/nnano.2017.4.
[44] C. Yang, X. Pan, X. Xu, C. Cheng, Y. Huang, L. Li, et al., Salvianolic acid C potently inhibits SARS-CoV-2 infection by blocking the formation of six-helix bundle core of spike protein, Signal Transduct. Targeted Ther. 1 (2020) 220, https://doi.org/10.1038/s41392-020-00335-z.
[45] Z. Zhu, P. Mesci, J.A. Bernatchez, R.C. Gimple, X. Wang, S.T. Schafer, et al., Zika virus targets glioblastoma stem cells through a SOX2-Integrin αvβ5 axis, Cell Stem Cell 2 (2020) 187–204.e10, https://doi.org/10.1016/j.stem.2019.11.016.
[46] C.V. Messias, J.P. Lemos, D.P. Cunha, Z. Vasconcelos, L.M.S. Raphael, M. C. Bonaldo, et al., Zika virus infects human blood mononuclear cells, BMC Infect. Dis. 1 (2019) 986, https://doi.org/10.1186/s12879-019-4596-9.
[47] S. Sen Santara, D.J. Lee, Á. Crespo, J.J. Hu, C. Walker, X. Ma, et al., The NK cell receptor NKp46 recognizes ecto-calreticulin on ER-stressed cells, Nature 6 (2023) 348–356, https://doi.org/10.1038/s41586-023-06952-2.
[48] R. Jeske, C. Liu, L. Duke, M.L. Canonicco Castro, L. Muok, P. Arthur, et al., Upscaling human mesenchymal stromal cell production in a novel vertical-wheel bioreactor enhances extracellular vesicle secretion and cargo profile, Bioact. Mater. 2 (2022) 732–747, https://doi.org/10.1016/j.bioactmat.2022.07.004.
[49] H. Huang, L. Xiao, L. Fang, M. Lei, Z. Liu, S. Gao, et al., Static topographical cue combined with dynamic fluid stimulation enhances the macrophage extracellular vesicle yield and therapeutic potential for bone defects, ACS Nano 9 (2025) 8667–8691, https://doi.org/10.1021/acsnano.4c15201.
[50] J.H. Lee, H. Jeon, J. Lötvall, B.S. Cho, Therapeutic potential of mesenchymal stem cell-derived extracellular vesicles in SARS-CoV-2 and H1N1 influenza-induced acute lung injury, J. Extracell. Vesicles 13 (2024) e12495, https://doi.org/10.1002/jev2.12495.
[51] Y. Wan, L. Li, R. Chen, J. Han, Q. Lei, Z. Chen, et al., Engineered extracellular vesicles efficiently deliver CRISPR-Cas9 ribonucleoprotein (RNP) to inhibit herpes simplex virus1 infection in vitro and in vivo, Acta Pharm. Sin. B 3 (2024) 1362–1379, https://doi.org/10.1016/j.apsb.2024.02.003.
[52] S. Li, H. Shu, The membrane-associated ubiquitin ligases MARCH2 and MARCH3 target TIM-1 to limit Zika virus infection, Cell. Mol. Immunol. 22 (2025) 1032–1044, https://doi.org/10.1038/s41423-024-01242-x.
[53] C. Cheng, H. Yang, C. Yang, et al., LATS2 degradation promoted fibrosis damage and rescued by vitamin K3 in lupus nephritis, Arthritis Res. Ther. 26 (2024) 64, https://doi.org/10.1186/s13075-024-03296-8.
[54] H.M. Lazear, J. Govero, A.M. Smith, D.J. Platt, E. Fernandez, J.J. Miner, et al., A mouse model of zika virus pathogenesis, Cell Host Microbe 5 (2016) 720–730, https://doi.org/10.1016/j.chom.2016.10.004.
[55] T. Singh, K.K. Hwang, A.S. Miller, R.L. Jones, C.A. Lopez, S.J. Dulson, et al., A Zika virus-specific IgM elicited in pregnancy exhibits ultrapotent neutralization, Cell 25 (2022) 4826–4840.e17, https://doi.org/10.1016/j.cell.2022.10.023.
[56] Z. Lei, Y. Gu, Y. Liu, H. Liu, X. Lu, W. Chen, et al., Identification of antiviral RNAi regulators, ILF3/DHX9, recruit at ZIKV stem loop B to protect against ZIKV induced microcephaly, Nat. Commun. 1 (2025) 1991, https://doi.org/10.1038/s41467-025-46277-w.